

Anisotropic amplitude variation of the bottom-simulating reflector beneath fracture-filled gas hydrate deposit

Sriram, G.¹, Dewangan, P.^{1*}, Ramprasad, T.¹, Rama Rao, P.²

¹ CSIR-National Institute of Oceanography, Dona Paula, Goa, 403004, India

² Andhra University, Vishakhapatnam, Andhra Pradesh, 530003, India

*Corresponding author email: pdewangan@nio.org

Abstract

For the first time, we report the amplitude variation with angle (AVA) pattern of bottom simulating reflectors (BSRs) beneath fracture-filled gas hydrate deposits when the effective medium is anisotropic. The common depth point (CDP) gathers of two mutually perpendicular multi-channel seismic profiles, located in the vicinity of Site NGHP-01-10, are appropriately processed such that they are fit for AVA analysis. AVA analysis of the BSR shows normal-incidence reflection coefficients of -0.04 to -0.11 with positive gradients of 0.04 to 0.31 indicating class IV pattern. The acoustic properties from isotropic rock physics model predict class III AVA pattern which cannot explain the observed class IV AVA pattern in Krishna-Godavari basin due to the anisotropic nature of fracture-filled gas hydrate deposits.

We modeled the observed class IV AVA of the BSR by assuming that the gas hydrate bearing sediment can be represented by horizontally transversely isotropic (HTI) medium after accounting for anisotropic wave propagation effects on BSR amplitudes. The effective medium properties are estimated using Backus averaging technique and the AVA pattern of BSRs is modeled using the properties of overlying HTI and underlying isotropy/HTI media with or without free gas. Anisotropic AVA analysis of the BSR from the inline seismic profile shows 5-30 % gas hydrate concentration (equivalent to fracture density) and the azimuth of fracture system (fracture orientation) with respect to the seismic profile is close to 45°. Free gas below the base of gas hydrate stability zone is interpreted in the vicinity of fault system (F1).

1. Introduction

Gas hydrate represents a solid crystalline form of lighter hydrocarbon gases trapped within the cages of water molecules. It is stable under high pressure and low temperature conditions within zones referred to as gas hydrate stability zone (GHSZ) [Sloan, 1990]. In marine sediments, gas hydrate occurs in various forms such as pore-filling, sediment matrix, fracture-filling, massive etc. The base of the GHSZ is manifested in seismic data in the form of bottom simulating reflector (BSR) which is formed due to the impedance contrast between the overlying gas hydrate and underlying water/free gas bearing sediments [Singh *et al.*, 1993]. Normally, BSR is identified in seismic data based on its characteristic signatures such as mimicking the seafloor, opposite polarity with respect to the seafloor reflection and cross-cutting the existing geological horizons [Hyndman and Spence, 1992; Singh *et al.*, 1993].

The presence of gas hydrate or free gas alters the physical properties of the background marine sediments. In general, the presence of gas hydrate within the GHSZ increases the P- and S-wave velocities, while free gas below the GHSZ decreases the P-wave velocity [Helgerud *et al.*, 1999]. Several rock physics theories have been proposed to explain the perturbation in elastic velocities and density depending on the distribution of the hydrate within the sediments and can also be used to estimate the saturations of gas hydrate and free gas [Lee *et al.*, 1996; Dvorkin *et al.*, 1999; Helgerud *et al.*, 1999; Lee and Collett, 2001; Lee, 2004, 2008; Lee and Collett, 2009]. The differences in the elastic velocities and densities across the GHSZ govern the amplitude variation with angle (AVA) of BSRs which can be studied from the multi-channel seismic data.

AVA patterns can be classified into four categories (I-IV) depending on the intercept and gradient [Ostrander, 1984; Castagna *et al.*, 1998]. The AVA pattern of BSRs is well established for isotropic media where gas hydrate occurs as pore-filling or as a load-bearing matrix [Ojha and Sain, 2007; Müller *et al.*, 2007]. In general, the presence of free gas below the GHSZ causes a large negative intercept and a negative gradient (class III AVA) [Andreassen *et al.*, 1997; Hyndman and Spence, 1992]. However, the rock physics model of Carcione and Tinivella [2000] shows a negative intercept and a positive gradient (class IV AVA) for high hydrate saturation (>40 %). For the first time, we classify AVA patterns of BSRs beneath fracture-filled gas hydrate deposits when the effective medium is anisotropic. We present a case study of the AVA pattern of a BSR in the KG offshore basin using available multi-channel seismic (MCS) data in the vicinity of Site NGHP-01-10.

The AVA analysis is supposed to examine the reflection coefficients at the target horizon; therefore, an essential element of AVA processing is to remove the known factors other than reflection that can affect the amplitude of the reflection. Another important factor in the AVA analysis is the choice of an appropriate rock-physics model that governs the relationship between the P- and S-wave velocities and density of the gas hydrate bearing sediment with the hydrate saturation, porosity and the elastic moduli of the matrix, pore fluid and hydrate [Müller *et al.*, 2007; Sava and Hardage, 2006].

2. Geological setting of gas hydrate deposits in the Krishna-Godavari (KG) offshore basin

The study area (Figure 1) is located in the KG offshore basin, eastern continental margin of India, which evolved as a consequence of rifting and subsequent drifting of the Indian plate away from the contiguous Antarctica-Australia plate [Scotese *et al.*, 1988; Ramana *et al.*, 2001]. The KG basin spreads over an area of ~28,000 km² onland, while its offshore extension encompasses an area of ~145,000 km² [Rao, 2001; Bastia, 2007]. The basin is characterized by echelon-type horst and graben like structures, and the grabens are filled with a thick pile of Permian to recent sediments [Rao and Mani, 1993; Rao, 2001; Gupta, 2006]. The Krishna and Godavari river systems discharge the bulk of detrital sediments into the KG basin.

The occurrence of gas hydrate in the KG offshore basin is inferred from the presence of BSRs in seismic data [Ramana *et al.*, 2006; Collett *et al.*, 2008; Dewangan *et al.*, 2010; Shankar and Riedel, 2010; Riedel *et al.*, 2010]. Gas hydrate-related proxies such as geophysical and geochemical signatures of fluid/gas migration, pockmarks, etc., are reported from the KG offshore based on the analysis of shallow sediment cores (~6 m) and geophysical data [Ramana *et al.*, 2008]. The presence of gas hydrate is confirmed by drilling/coring during expedition NGHP-01 onboard JOIDES resolution [Collett *et al.*, 2008]. The detailed analyses of multibeam bathymetry, high resolution sparker and multi-channel seismic data indicated several topographic mounds in the KG offshore basin which are formed due to neo/shale tectonic activities [Dewangan *et al.*, 2010]. These mounds are heavily faulted and show seismic signatures of fluid/gas movement and hence are the probable locations for gas hydrate accumulation and formation of cold seeps. The multi-channel seismic (MCS) data used in the present study are acquired in the vicinity of Site NGHP-01-10 where ~128 m fracture-filled gas hydrate deposit is confirmed by drilling/coring [Collett *et al.*, 2008]. Detailed analysis of the MCS data for structures, velocity models and BSR-derived geothermal gradient suggests that the gas hydrate is distributed along the fracture zones due to the migration of fluid/gas through the fracture system [Dewangan *et al.*, 2011].

3. Seismic Data

The high resolution multi-channel seismic (MCS) data used in the present study were acquired by Oil and Natural Gas Commission Ltd. (ONGC) in the KG offshore basin for oil/gas exploration. A 1000 cu. in. air gun was used as a seismic source and the shots were fired at an interval of 12.5 m. The seismic data were recorded using a hydrophone steamer of 1.5 km length with a receiver interval of 12.5 m. The near- and far-offsets of the seismic data are 75 and 1575 m, respectively. The data were recorded digitally at a sampling interval of 1 ms with a record length of 4 s after applying 500 Hz high-cut anti-alias filter. Two lines, which are perpendicular to each other in the vicinity of Site NGHP-01-10, are used in the present study. The seismic profile oriented in NNW-SSE direction is referred to as inline, while the profile oriented in ENE-WSW direction is referred to as crossline (Figure 1).

4. Seismic data processing for AVA analysis

A typical processing sequence for multi-channel seismic data includes bandpass filtering, spherical divergence correction, spiking deconvolution, velocity analysis, stacking and post-stack time migration. In addition, a constant static correction is also applied so that the zero-offset travel time of the seafloor multiple is twice that of the seafloor. The time-migrated sections of inline and crossline seismic profiles are shown in Figure 2. The BSR is observed around 1.58-1.65 s two way travel time (TWT) in the inline seismic profile and around 1.6-1.8 s TWT in the crossline profile (Figure 2). The variation in BSR amplitudes on stacked data has been correlated with the occurrence of gas hydrate deposits and fault system [Dewangan *et al.*, 2011]. In the present study, we attempt to understand the pattern of the BSR amplitudes in the pre-stack seismic data.

We adopted an established methodology for preprocessing of seismic data for AVA analysis [Hyndman and Spence, 1992; Andreassen *et al.*, 1995, 1997; Dewangan and Ramprasad, 2007]. After assigning geometry to the raw seismic data, the following preprocessing sequence was carried out: band pass filter (20-30-200-220 Hz) was applied to remove the low and high frequency noise in the seismic data, spherical divergence correction was applied by multiplying the amplitudes of seismic data with the product of time and square of root mean squared (RMS) velocity [Newman, 1973] and spiking deconvolution was applied to minimize the effect of the variation in source wavelet due to seismic attenuation.

The near-offset (75-295 m) and far-offset (1295-1545 m) stack of the processed seismic data for the inline and crossline seismic profiles are shown in Figures 3 and 4, respectively. The BSR amplitudes

show significant variation with CDP and offset. Two distinct amplitude variation with offset (AVO) patterns of BSR are observed in the seismic data. Large BSR amplitudes are observed in the near-offset stack (Figure 3a) between CDPs 350 and 480 and the absolute values of the BSR amplitudes for the corresponding CDPs decrease in the far-offset stack (Figure 3b). A similar reduction in BSR amplitudes with offset is observed for CDPs 500-550, 620-660 and 780-850; however, for these CDPs the BSR amplitude is moderate in near-offset stack and is very weak in far-offset stack. Such an AVO pattern of the BSR represents a class IV amplitude anomaly. Similarly, we observe large-to-moderate BSR amplitudes in near-offset stack (Figure 4a) between CDPs 480-550 and 680-780 and a weak BSR in the far-offset stack (Figure 4b) in the crossline seismic sections representing class IV AVO anomaly. In contrast, a weak BSR is observed in the near-offset stack of the inline seismic section (Figure 3a) for CDPs 710-760, and the absolute values of the amplitudes for these CDPs increase in the far-offset section representing class II/III AVO anomaly.

In order to further investigate the AVO pattern of the BSR, the amplitudes of BSR and seafloor were extracted from the seismic data. The isotropic velocity model obtained from conventional semblance analysis [Dewangan *et al.*, 2011] and the zero-offset travel times of seafloor and BSR were used to compute the travel times as a function of offset using the hyperbolic normal moveout (NMO) equation. The amplitudes corresponding to BSR and seafloor travel times were extracted from the processed pre-stack seismic data. The extracted seafloor and BSR amplitudes are corrected for the receiver directivity [Sheriff and Geldart, 1982]. The zero-offset seafloor reflection coefficient (R_{SF}) is calculated from the ratio of the amplitudes of seafloor multiple (A_m) and seafloor (A_p) after applying the spherical divergence correction [Warner, 1990],

$$R_{SF} = \frac{A_m}{A_p} \cdot \quad (1)$$

Similarly, the zero-offset reflection coefficient of BSR (R_{BSR}) is obtained as

$$R_{BSR} = \frac{A_{BSR}}{A_p} \frac{R_{SF}}{(1 - R_{SF}^2)}. \quad (2)$$

In AVO studies, source directivity is critical as it can significantly distort the amplitudes at far offsets and may lead to misinterpretation. Source directivity can be corrected if any independent information is available [Müller *et al.*, 2007]. In the absence of such information, the source directivity correction is carried out by calibrating the seafloor amplitude with reference to seafloor AVO response

obtained from well log parameters [Andreassen et al., 1997; Ecker et al., 1998]. The seafloor AVO is calculated using the Zoeppritz equations [Zoeppritz, 1919] from the properties of the water column obtained from CTD data ($V_{p1}=1.47$ km/s, $V_{s1}=0.0$ km/s, $\rho_1=1.030$ g/cm³) and from the properties of the sea-bottom obtained from logging while drilling (LWD) data at Site NGHP-01-10 ($V_{p2}=1.47$ km/s, $V_{s2}=0.160$ km/s, $\rho_2=1.46$ g/cm³). The same normalization factor is applied to the BSR amplitudes at all offsets. In order to express the seafloor amplitudes as a function of incidence angle (θ), the offset distance (x) is converted to the incidence angle using the equation,

$$\theta = \tan^{-1}\left(\frac{x}{2z}\right), \quad (3)$$

where z represents the depth to the seafloor. The incidence angles of the BSR are estimated by isotropic ray-tracing in a two-layered horizontal model where the average interval velocity of the gas hydrate bearing sediment is estimated to be ~ 1600 m/s based on conventional semblance analysis [Dewangan et al., 2011]. The reflection coefficients expressed in terms of incidence angle hereinafter are termed as amplitude variations with angle (AVA).

5. Results: AVA of BSR in the KG offshore basin

The reflection coefficients of the seafloor and BSR for a group of 5-6 CDPs are shown in Figure 5. Due to normalization of the seafloor amplitudes, the mean value of the seafloor reflection coefficients matches with that estimated from the elastic velocities and densities of water column and sea-bottom sediments. The intercept (A) and the gradient (B) of the BSR reflection coefficients are estimated by fitting the data with the three-term Shuey's approximation $R_{pp}(\theta) = A + B \sin^2(\theta) + C \sin^2(\theta) \tan^2(\theta)$ to the Zoeppritz equations [Shuey, 1985]. The BSR reflection coefficients in the vicinity of CDPs 835 (inline) and 715 (crossline) are small (-0.04) at normal-incidence and their absolute values decrease with a small gradient of ~ 0.04 representing class IV AVA (Figures 5a and 5b). Similarly, the BSR reflection coefficients for the CDPs 430 (inline) and 520 (crossline) are moderate (-0.08 to -0.11) at normal-incidence and their absolute values decrease with a gradient of ~ 0.3 representing class IV AVA pattern (Figures 5c and 5d). Several gathers in the vicinity of CDPs 396, 480, 510, 643 (inline) and 777, 790 (crossline) show similar class IV AVA with low-to-moderate normal-incidence reflection coefficients and positive gradients. We attempt to model the observed class IV AVA pattern of the BSR using the established rock-physics models in the KG offshore basin.

6. Discussion

6.1 Modeling of observed class IV AVA of BSR in the KG offshore basin

The class IV AVA pattern of BSRs is known for high gas hydrate saturation (> 40-45 %) with or without the presence of free gas below the base of GHSZ [Carcione and Tinivella, 2000]. Such an AVA pattern has been reported for Berea sandstone in a permafrost environment where the background P- and S-wave velocities are 2.0 and 0.75 km/s, respectively and increase to 4.5 and 3.0 km/s for 100 % gas hydrate saturation. However, in the KG offshore basin, the observed P- and S-wave background velocities are 1.503 and 0.166 km/s, respectively [Collett et al., 2008; Lee and Collett, 2009], therefore the assumption of the rock-physics model of Carcione and Tinivella [2000] may not be applicable for the KG offshore basin.

The three-phase Biot-type equation (TPBE) [Lee and Waite, 2008] predicts the background P- and S-wave velocities of the marine sediment in the KG offshore basin at Site NGHP-01-10 [Lee and Collett, 2009]. Therefore, the TPBE model is used in the present study. The TPBE model (Appendix A) is defined for the consolidated marine sediments based on the empirical relation between the dry frame moduli and the matrix moduli [Pride, 2003; Pride et al., 2004]. The model depends on the consolidation parameter (α), which is a function of effective pressure and the degree of consolidation. This parameter can be obtained by comparing the observed P-wave velocities with those estimated from TPBE. Based on the empirical relation at Site NGHP-01-10, Lee and Collett [2009] estimated the consolidation

parameter (α) as a function of depth (d); $\alpha = 70 \left(\frac{200}{d} \right)^{\frac{1}{3}}$. The predicted P- and S-wave velocities from

TPBE model match with the observed background velocities of 1.503 and 0.166 km/s, respectively and the density of the sediments is estimated to be 1.563 g/cm³. The TPBE model is also used to estimate the P- and S-wave velocities and density of gas hydrate bearing sediments by incorporating gas hydrate as a part of sediment matrix. The parameter ω (Appendix A) accounts for the reduced impact of hydrate formation relative to compaction in terms of stiffening the host sediment framework and its recommended value for modeling the gas hydrate bearing sediments is 0.12 [Lee and Waite, 2008]. The P- and S-wave velocities increase with gas hydrate saturation to 3 and 0.9 km/s, respectively for 100 % hydrate saturation and 65 % porosity (Figure 6a).

6.2 AVA pattern of BSR using TPBE model

The AVA of BSRs is computed using the Zoeppritz equations [Zoeppritz, 1919] with the elastic parameters estimated from the TPBE model for different gas hydrate saturations (Figure 6b). The presence of free gas below the BSR yields a large normal-incidence reflection coefficient with class III AVA rather than class IV AVA [Carcione and Tinivella, 2000; Sava and Hardage, 2006]; therefore, no free gas is assumed below the BSR for the TPBE model. The magnitude of the normal-incidence reflection coefficient increases with hydrate saturation as the velocities of hydrate-bearing sediments increase with hydrate saturation (Figure 6b). We observed that the computed reflection coefficients show a class III AVA pattern and the absolute value of the intercept as well as the gradient increases with hydrate saturation. Therefore, the TPBE model fails to explain the observed class IV AVA of BSRs in the KG offshore basin.

In general, a class IV AVA pattern is governed by a significant perturbation in S-wave velocity [Hardage *et al.*, 2007]. Therefore, we studied the approximate condition which may lead to class IV AVA in isotropic media (Appendix B). For positive AVA gradients of BSRs, the following condition is derived assuming small contrasts in the elastic velocities and constant density across the base of the GHSZ,

$$\left| \frac{8\bar{\beta}}{\bar{\alpha}} \right| > \left| \frac{\Delta\alpha}{\Delta\beta} \right|, \quad (4)$$

where $\bar{\alpha}$ and $\bar{\beta}$ are the average P- and S-wave velocities for the upper and lower layers, respectively. The parameters $\Delta\alpha$ and $\Delta\beta$ represent the contrasts in P- and S-wave velocities across the GHSZ. In order to span all possible combinations of P- and S-wave velocities that can lead to a class IV AVA pattern in an isotropic medium, we perform the following calculations; a) estimate the P- and S-wave velocities of the gas hydrate bearing sediment (GHBS) by arbitrary perturbation of the background velocities, b) compute the reflection coefficients of the BSR using the Zoeppritz equations assuming constant density across the base of the GHSZ as the presence of gas hydrates does not significantly alter the density of the sediments, and c) estimate the AVA gradient by fitting the computed reflection coefficients with the three-term Shuey's approximation. The AVA gradient is shown as a function of P- and S-wave velocity contrasts (Figure 7). The approximate condition for the zero-gradient (equation B3) is close to the computed zero-gradient suggesting that it remains accurate even for large velocity contrasts. Equation

(4) suggests that class IV AVA in isotropic medium is possible when the ratio of the differences of the P- and S-wave velocities is less than eight times the ratio of the average P- and S-wave velocities. Thus, the class IV AVA pattern is more likely for sediments with high background S-wave velocity and for hydrate distribution with relatively large S-wave velocity contrast compared to that of P-wave.

The TPBE model fails to predict the observed class IV AVA of BSRs in the KG offshore basin as it estimates low S-wave velocities for different hydrate saturations (Figure 6a). Independently, *Lee and Collett* [2009] observed that TPBE model is overestimating the hydrate saturation in the KG offshore basin (40-50 %) as compared to that observed from the pressure cores (20-25%) and suggested that this difference is caused by the anisotropy of the GHBS. Furthermore, the X-ray images of the pressure cores of the GHBS show numerous sub-horizontal and high angle fracture-filled hydrate which can be modeled as anisotropic medium. We model the observed class IV AVA of the BSR using the available anisotropic rock physics theories in the KG offshore basin.

6.3 Anisotropy due to fracture-filled gas hydrate

The distribution of gas hydrates is often governed by lithology; for example, they get preferentially deposited in the sandy layers at the Mallik site [*Dallimore et al.*, 1999] and in the Nankai trough [*Matsumoto et al.*, 2001] and within the coarse ash-layers in the Andaman basin [*Collett et al.*, 2008]. The gas hydrate accumulation may also be governed by structure controls; for example, hydrate gets preferentially deposited in the fault/fracture network in the KG offshore basin [*Collett et al.*, 2008; *Dewangan et al.*, 2011; *Jaiswal et al.*, 2012a,b]. Such fracture-filled deposits may exhibit significant lateral heterogeneity. The aligned fracture-filled gas hydrate can be modeled as an effective anisotropic medium in seismic data. Such anisotropy due to gas hydrates has been reported from Hydrate Ridge [*Kumar et al.*, 2006] and the KG offshore basin [*Lee and Collett*, 2009; *Cook et al.*, 2010]. The anisotropy of GHBS in the KG offshore basin has led to a mismatch between the hydrate saturation estimated from sonic logs using the TPBE model and that estimated from pressure cores.

There are two competing anisotropic rock physics models for GHBS in the KG offshore basin. The model proposed by *Lee and Collett* [2009] suggests that the P- and S-wave velocities of the GHBS can be estimated by assuming that the fractured medium is composed of two layers of different volume fractions. The first component is parallel fractures filled with 100 % gas hydrate, while the second component is an isotropic medium whose elastic velocities and density are given by 100 % water-saturated sediments. When the layer thicknesses are much smaller than the seismic wavelength, the

effective medium behaves as transversely isotropic with symmetry axis oriented normal to the layering [Backus, 1962; White, 1965]. The fractures are assumed to be rotationally invariant and the coupling between the normal and tangential stiffness is negligible which yields an HTI medium [Bakulin *et al.*, 2000a]; otherwise, the effective medium exhibits lower anisotropic symmetry such as monoclinic even for single set of vertical fractures [Bakulin *et al.*, 2000b]. An alternative model proposed by Ghosh *et al.*, [2010] suggests that the background clay-rich sediment is intrinsically anisotropic due to the orientation of the clay platelets and behaves as a VTI (TI with a vertical symmetry axis) medium. They incorporated fracture-filled gas hydrate in the background VTI medium using differential effective medium (DEM) theory [Jakobsen *et al.*, 2000] which yields an orthorhombic medium. The coefficients of the orientation distribution function (ODF) W_{200} and W_{400} [Johansen *et al.*, 2004], which represent the strength of the background VTI medium, were obtained by matching the background P- and S-wave velocities at Site NGHP-01-03 (a hydrate free site) with those calculated from the combined self-consistence approximation (SCA)-DEM theory. The estimated values of the ODF coefficients ($W_{200} = 0.033$ and $W_{400} = 0.0383$) suggest a VTI medium with $\varepsilon = 0.21$ and $\delta = -0.04$ [Johansen *et al.*, 2004]. The parameter ε represents the fractional difference between the horizontal and vertical P-wave velocities, and δ represents the normalized second derivative of P-wave phase velocity at vertical incidence [Thomsen, 1986].

In order to decide whether the background medium can be considered as VTI for seismic modeling, we looked into the long-offset seismic data (offset-to-depth ratio ~ 4.7 ; Figure 8a) in the vicinity of Site NGHP-01-03 [Collett *et al.*, 2008]. The BSR, which is probably formed due to the presence of free gas below the base of GHSZ, is observed clearly in the seismic section. The CDP gather in the vicinity of Site NGHP-01-03 is corrected for normal moveout (NMO) assuming hyperbolic travel time (Figure 8b). The reflections corresponding to the seafloor (1.4 s), BSR (1.7 s) and a deeper horizon (2.2 s) are almost flat indicating that their moveouts are approximately hyperbolic. If the background medium is VTI, the moveout will be non-hyperbolic; however, no evidence of non-hyperbolic moveout is observed in the CDP gather. We computed the travel time using anisotropic ray tracing for a two-layered horizontal medium; isotropic water column and the background VTI medium with the parameters given by Ghosh *et al.*, [2010]. The computed travel time for an effective VTI medium is shown in Figure 8b after hyperbolic moveout correction. No indication of anisotropy is observed in the seismic data suggesting that the background sediments can be considered as an isotropic medium. Therefore, we follow Lee and Collett [2009] to estimate the effective medium properties of the gas

hydrate bearing sediment in the KG offshore basin using the Backus averaging technique [Backus, 1962; Appendix C]. The effective anisotropic parameters are estimated from the properties of 100 % fracture-filled hydrate ($V_{p1}=3.744$ km/s, $V_{s1}=0.1946$ km/s $\rho_1=0.926$ g/cm³), 100 % water saturated sediment estimated from TPBE model at an average porosity of 65 % ($V_{p2}=1.503$ km/s, $V_{s2}=0.166$ km/s and $\rho_2=1.563$ g/cm³), and the volumetric fraction of the hydrate layer (hydrate concentration). The effective medium thus obtained will be transversely isotropic with symmetry axis oriented normal to the layers. X-ray images of the pressure cores show near vertical fractures in the KG offshore basin which can be modeled as an HTI (TI with a horizontal symmetry axis) medium. Therefore, we assume that the axis of symmetry lies in the horizontal plane to simulate vertical fractures. As shown by Lee and Collett [2009], such an HTI medium predicts the gas hydrate saturation accurately at Site NGHP-01-10. In HTI medium, the P-wave propagating along the direction of hydrate layers will have a higher velocity than that traveling perpendicular to the hydrate layers. Further, S-waves propagating parallel to the layers split into two distinct S-waves. The S-wave polarized parallel to the hydrate layers has higher velocity than that polarized in the perpendicular direction, which results in shear-wave splitting [Thomsen, 1988].

6.4 AVA of BSR beneath an anisotropic fracture-filled gas hydrate deposit

The fracture-filled gas hydrate deposit is assumed to be represented by an HTI medium. The symmetry axis of the HTI medium is assumed to be in x_1 -direction and the x_3 axis is vertical. The $[x_1, x_3]$ -plane, which contains the symmetry axis, is referred to as the “symmetry-axis plane”, while the $[x_2, x_3]$ -plane, which is along the strike direction of the fault plane, is referred to as the “isotropy plane”. The waves propagating in the isotropy plane do not exhibit any velocity variation with angle. In order to understand the effect of anisotropy on AVA, the stiffness matrix is computed for different gas hydrate concentrations and the coefficients of the matrix are expressed in terms of Thomsen-style anisotropic parameters $\delta^{(V)}$, $\varepsilon^{(V)}$, and $\gamma^{(V)}$ for HTI media (Figure 9) [Tsvankin, 1997; Rüger, 1997] as the former do not provide much insight into the anisotropic effect on the reflection coefficients. The vertical P-wave velocity ($\alpha = \sqrt{C_{33} / \rho}$) increases with the gas hydrate concentration (GHC) reaching a maximum of 3.744 km/s for pure hydrate. The corresponding P-wave velocity from the isotropic TPBE model is close to the horizontal P-wave velocity ($\alpha^\perp = \sqrt{C_{11} / \rho}$). The fast S-wave at vertical incidence is polarized in the isotropy plane and its velocity ($\beta = \sqrt{C_{44} / \rho}$) increases rapidly with the hydrate concentration reaching a maximum of 1.946 km/s for pure hydrate. On the other hand, the velocities of the slow S-

wave ($\beta^\perp = \sqrt{C_{55}/\rho}$) polarized in the symmetry-axis plane increase slowly with the GHC. The corresponding S-wave velocities obtained from the TPBE model are close to that of the slow S-wave in the HTI model (Figure 9b). The parameter $\varepsilon^{(v)}$ represents the fractional difference between the horizontal and vertical P-wave velocities in the symmetry-axis plane and shows systematic variation reaching a minimum value of -0.15 at 50 % GHC (Figure 9d). The parameter $\delta^{(v)}$ represents the normalized second derivative of the P-wave phase velocity in the $[x_1, x_3]$ -plane at vertical incidence and decreases with hydrate concentration reaching a minimum value of -0.38 at 85 % GHC (Figure 9e). The parameter $\gamma^{(v)}$ represents the fractional difference between the horizontal and vertical SH-wave velocities in the symmetry-axis plane and decreases rapidly with gas hydrate concentration attaining a minimum value of -0.45 at 20% GHC (Figure 9f). It increases rapidly towards zero when the hydrate concentrations exceed 80 %. The shear wave splitting parameter (γ) is close to the fractional difference between the fast and slow vertical S-wave velocities at vertical incidence and increases rapidly to a maximum of 6.3 at 50 % GHC (Figure 9c). The parameter $\gamma^{(v)}$ can be represented in terms of γ using the relationship; $\gamma^{(v)} = \frac{-\gamma}{1+2\gamma}$.

The AVA of the BSR is assumed to be caused due to the overlying HTI medium and the underlying background isotropic medium without free gas. The reflection coefficients vary with both the incidence phase angle and the azimuth which is defined with respect to the symmetry-axis plane [Rüger, 1998; Jilek, 2001]. It can be calculated using the anisotropic Zoeppritz equations [Vavryčuk and Pšenčík, 1998; Vavryčuk, 1999; Jilek, 2001] with the parameters estimated from the Backus model. In order to gain insight into the influence of anisotropy parameters on AVA, we employ the weak-anisotropy approximation for the P-wave reflection coefficients [Rüger, 1998],

$$R_p(i, \phi) = \frac{1}{2} \frac{\Delta Z}{\bar{Z}} + \frac{1}{2} \{B^{iso} + B^{ani} \cos^2 \phi\} \sin^2 i + \frac{1}{2} \left\{ \frac{\Delta \alpha}{\bar{\alpha}} + \Delta \varepsilon^{(v)} \cos^4 \phi + \Delta \delta^{(v)} \sin^2 \phi \cos^2 \phi \right\} \sin^2 i \tan^2 i, \quad \text{where } i \text{ is the incidence phase angle and } \phi \text{ is the azimuth. } Z \text{ denotes the vertical P-wave impedance, while } G \text{ represents the shear modulus for the vertically propagating fast S-wave } (\beta). \text{ The average P-wave impedance of the upper and lower layers is given by } \bar{Z}, \text{ while the difference is denoted by } \Delta Z.$$

$$B^{iso} = \frac{\Delta \alpha}{\bar{\alpha}} - \left(\frac{2\bar{\beta}}{\bar{\alpha}} \right)^2 \frac{\Delta G}{G}, B^{ani} = \Delta \delta^{(v)} + 2 \left(\frac{2\bar{\beta}}{\bar{\alpha}} \right)^2 \Delta \gamma, \quad \text{denotes}$$

the incidence phase angle and ϕ is the azimuth. Z denotes the vertical P-wave impedance, while G represents the shear modulus for the vertically propagating fast S-wave (β). The average P-wave impedance of the upper and lower layers is given by \bar{Z} , while the difference is denoted by ΔZ .

Similarly, the average shear modulus is denoted by \bar{G} , while the difference is denoted by ΔG . The exact P-wave reflection coefficients are computed as a function of incidence phase angle in the symmetry-axis and isotropy planes for different hydrate concentrations (Figure 10). In the isotropy plane, the P-wave reflection coefficients show positive gradients for different hydrate concentrations. The AVA gradient in the isotropy plane of an HTI medium (B^{iso}) is represented by the same functional dependence as that of an isotropic medium, but it is governed by the vertical velocity of the fast shear wave (β) which is much larger than that of slow shear wave (β^\perp). Due to this large contrast in the shear modulus (ΔG), the HTI medium can generate class IV AVA pattern for different hydrate concentrations in the isotropy plane. Since the phase and group angles are same in the isotropy plane, such class IV AVA patterns remain valid even for the incidence group angle.

The AVA gradient in the symmetry-axis plane of the HTI medium ($B^{sym} = B^{iso} + B^{ani}$) can be simplified by following Rüger [1998],

$$B^{sym} = \frac{\Delta\alpha}{\bar{\alpha}} - \left(\frac{2\beta^\perp}{\bar{\alpha}} \right)^2 \frac{\Delta G^\perp}{\bar{G}^\perp} + \Delta\delta^{(V)}. \quad (6)$$

The AVA gradient in the symmetry-axis plane is governed by the vertical velocity of the slow shear wave (β^\perp), which is close to the S-wave velocity estimated from the TPBE model, and the contribution from the contrast of the anisotropy parameter $\Delta\delta^{(V)}$. The parameter $\Delta\delta^{(V)}$ is positive and the AVA gradient from the TPBE model is negative for different hydrate concentrations (Figure 6b); their sum leads to an overall small AVA gradient as observed in Figure 10a. This inference remains qualitatively valid even if the reflection coefficients are expressed in terms of incidence group angle. The gradient for other azimuths (ϕ) can be obtained from equation (5).

6.5 Anisotropic AVA analysis in the KG offshore basin

The conventional processing sequence for the analysis of AVA is well established for isotropic media. However, if the medium is anisotropic due to fracture-filled gas hydrate deposits, the conventional processing sequence needs to be re-examined to account for anisotropy. The receiver directivity correction depends on the receiver array and is independent of subsurface model. Likewise, spiking deconvolution is data driven and also independent of the model. The source directivity correction depends on the reflection amplitudes of the seafloor. In the KG offshore basin, the presence of gas hydrate is not observed immediately below the seafloor; therefore, the source directivity correction is considered to be independent of anisotropy. The geometrical spreading in anisotropic

medium can significantly distort the amplitude of the target reflector [Ursin and Hokstad, 2003]. The most straightforward way to compute geometrical spreading is through dynamic ray tracing. However, the method requires accurate knowledge of anisotropic heterogeneous velocity field which is seldom available in practice. An alternate approach more suitable for AVO processing is based on the relationship between the geometrical spreading and reflection travel times. As shown by Xu *et al* [2005], the geometrical spreading factor L of pure modes (the amplitude decay as $1/L$) in an arbitrary anisotropic, laterally homogeneous medium can be expressed through the spatial derivatives of the travel time (T) of the reflected wave,

$$L^{-1}(x, \phi) = (\cos \varphi^s \cos \varphi^r)^{-1/2} \times \left[\frac{\partial^2 T}{\partial x^2} \frac{\partial T}{\partial x} \frac{1}{x} + \frac{\partial^2 T}{\partial x^2} \frac{\partial^2 T}{\partial \phi^2} \frac{1}{x^2} - \left(\frac{\partial T}{\partial \phi} \right)^2 \frac{1}{x^4} \right]^{\frac{1}{2}}, \quad (7)$$

where x is the source-receiver offset, ϕ is the azimuth of source-receiver line defined with respect to the symmetry axis, and φ^s and φ^r represent the incidence and the reflection group angles at the source and the receiver locations, respectively. In the case of anisotropic media with a horizontal plane of symmetry, the incidence and reflection group angles are equal ($\varphi^s = \varphi^r = \varphi$).

In order to simulate the geometrical spreading in anisotropic gas hydrate bearing sediment, the travel times of the BSR (T) are computed as a function of offset and azimuth using anisotropic ray tracing [e.g., Gajewski and Pšenčík, 1987]. We assume a two-layered model; the first layer is the isotropic water column of constant thickness of 1038 m and the second layer is the HTI medium of constant thickness of 140 m as observed in the log data of Site NGHP-01-10. The anisotropic parameters of the HTI medium are estimated using the Backus model for a particular hydrate concentration. The spatial derivatives of travel times are computed numerically and substituted in equation (7) for the estimation of amplitude decay. An isotropic geometrical spreading correction of $t \times V_{rms}^{-2}(\phi)$ has been applied to reflection amplitudes in anisotropic medium and the results are shown for the symmetry-axis, 45° azimuthal and the isotropy planes (Figure 11). As expected, the geometrical spreading correction is accurate for all offsets in isotropic medium. However, the isotropic geometrical-spreading correction underestimates the spreading in the symmetry-axis plane and overestimates in the isotropy plane due to the combination of 2D and 3D focusing effects in anisotropic medium [Tsvankin, 2001]. The effect of anisotropy in geometrical spreading correction is observed for the zero-incidence reflection coefficient. However, its effect on gradient can be ignored if the thickness of GHSZ is sufficiently small when compared to that of water column.

Anisotropy also affects the offset to group angle conversion and can be accounted by anisotropic ray tracing in a two-layered model: isotropic water column overlying an HTI medium. The offset to group angle conversion is a function of both the azimuth and the hydrate concentration. Our numerical test suggests that the incidence group angle changes dramatically with the azimuth and can significantly distort the AVA gradient. In the symmetry-axis plane, the velocity in the vertical direction is higher than that in the horizontal direction; as a result, the ray travels close to vertical direction even for large offsets and leads to smaller group angle. In contrast, severe ray bending occurs in the isotropy plane due to high velocity leading to large group angles for small offsets. Therefore, the conversion of offset to group angle cannot be ignored in an anisotropic medium.

The class IV AVA of BSRs shows low-to-moderate normal-incidence reflection coefficients ranging from -0.04 to -0.11 and positive AVA gradients from 0.04 to 0.3 (Figure 5). The analysis of structures in the 2D seismic data [Dewangan *et al.*, 2011] and 3D seismic data [Riedel *et al.*, 2010] shows the presence of fault systems (F1-F4) oriented in the NNW-SSE direction. The inline seismic profile is oriented at $\sim 40^\circ$ with respect to the symmetry axis of the fault system, and the crossline seismic profile is oriented at $\sim 45^\circ$. If the BSR reflection coefficient is modeled as a function of group angle using an approximate azimuth of 45° and a realistic estimate of the hydrate concentration of 10-30 % without free gas, the observed reflection coefficients for both the inline and crossline seismic profiles (Figure 12) can be predicted. The reflection amplitudes have been corrected for anisotropic geometrical spreading and the offset to group angle conversion has been achieved using an azimuth of 45° and the estimated hydrate concentration. The estimated hydrate concentrations are close to those observed from the pressure cores [Collett *et al.*, 2008] and the previously reported anisotropic rock physics model at Site NGHP-01-10 [Lee and Collett, 2009]. Our assumption of modeling the AVA pattern without free gas is supported by the drilling/coring data at Site NGHP-01-10 where no evidence of free gas below the base of GHSZ has been reported.

6.6 AVA of BSR in HTI/HTI media

The presence of free gas below the base of the GHSZ can decrease the P-wave velocity significantly, which in turn can modify the BSR reflection coefficient. We study the AVA due to the overlying fracture-filled gas hydrate and underlying fracture-filled free gas bearing sediment. The Biot-Gassmann theory modified by Lee [BGTL; Lee, 2004] has been used to estimate the velocities of the free gas bearing sediment. The Biot coefficient and the exponent value are assumed to be 0.9971 and

1.1, respectively. The calibration coefficient is assumed to be 5. These parameters work well for patchy gas saturation [Lee, 2004]. Similar to modeling of fracture-filled gas hydrate layer, the Backus average [Backus, 1962] is used to estimate the effective medium properties of fracture-filled free gas bearing sediment which depend on the properties of free gas bearing sediments with saturations 0-10 %, the properties of water saturated sediments and the volume fraction of free gas bearing sediment (fracture density). The resultant effective medium will thus be transversely isotropic. The axis of symmetry is assumed to lie in the horizontal plane to simulate vertical fractures. The BSR reflection coefficients from such an overlying fracture-filled gas hydrate and underlying fracture-filled free gas bearing sediment (both HTI media) are shown in Figure 13 for different hydrate concentrations and gas saturations. The volume fraction of free gas bearing sediment is assumed to be same as the hydrate concentration to simulate the same fracture density. The normal-incidence reflection coefficient as well as the gradient increases with the hydrate concentration and free gas saturation. The observed class IV AVA of BSR can also be modeled for a range of gas saturations (0-10 %) and hydrate concentrations (10-20 %) suggesting that AVA inversion is non-unique in the presence of free gas.

6.7 Application of AVA technique for fracture characterization

In an isotropic medium, the AVA study of BSRs helps in understanding the hydrate and free gas system in the vicinity of GHSZ [Hyndman and Spence, 1992]. Under the constraint of a suitable rock physics model, the AVA study can also be used to estimate hydrate and gas saturations as well as the V_p/V_s ratio of the gas hydrate bearing sediment [Ojha and Sain, 2007]. In this paper, we have extended the AVA study of BSRs to anisotropic media, in which BSRs are assumed to be formed due to a single set of gas hydrate filled, rotationally invariant, vertical faults/fractures. We demonstrate the application of the AVA technique to understand the fracture parameters from the inline seismic profile in the KG offshore basin (Figure 2a).

The amplitudes of the BSR were extracted from CDP gathers and P-wave reflection coefficients were estimated as a function of incidence angle after applying isotropic AVA processing. In case of limited offsets (offset-to-depth ratio is less than 1.5); only intercept (A) and gradient (B) can reliably be estimated from the seismic data by fitting the reflection coefficients with two-term Shuey's approximation. The normal-incidence P-wave reflection coefficients and isotropic gradients of selected CDPs across major fault zones are shown in Figures 14b and 14c, respectively. Positive gradients are observed for CDPs 390-510, 620-645, and 825-850 suggesting the class IV AVA pattern. These CDPs

are in the vicinity of regional fault systems F1, F3, and F5 as interpreted from 2D seismic data [Dewangan, *et al.*, 2011]. The normal-incidence reflection coefficients and gradients for these CDPs show positive correlation, i.e., an increase in absolute value of the reflection coefficient leads to an increase in gradient and vice versa. The class IV AVA pattern in HTI media is governed by three parameters: the hydrate concentration (equivalent to fracture density), gas saturation, and the azimuth of the symmetry axis (fracture azimuth) with respect to the orientation of the seismic line. The inversion of AVA parameters, normal-incidence reflection coefficient and gradient, is non-unique in the absence of any *a priori* information about the fracture azimuth or free gas saturation below the base of GHSZ.

We attempt to invert the medium parameters under the assumption of no free gas below the base of GHSZ. Our assumption is based on the available drilling/coring data (NGHP-01-10) in the study area [Collett *et al.*, 2008]. In order to account for anisotropic wave propagation effects such as geometrical spreading and offset to group angle conversion, the knowledge of HTI medium parameters as well as the fracture azimuth is required. The HTI medium parameters are obtained from the Backus model for a range of plausible hydrate concentrations ranging from 0 to 50 %. Similarly, the offset to group angle conversion is obtained using anisotropic ray-tracing in a two-layered model: an isotropic water column overlying HTI medium for a range of fracture azimuths (0° to 90°). The hydrate concentration and fracture azimuth can be estimated by matching the observed AVA parameters with those estimated from the anisotropic Zoeppritz equations and are shown in Figures 14d and 14e, respectively. The gas hydrate concentration within the fault zone F1 varies from 5 to 45 % with prominent peaks at CDPs 400 and 450. Interestingly, the maximum throw across the fault system is observed at CDP 450 which can be considered as the centre of the fault zone (Figure 2a). The gas hydrate concentration (fracture density) appears to be distributed symmetrically about the main fault F1. The mean azimuth of the fault systems is $\sim 45^\circ$ which is close to that interpreted from 2D seismics [Dewangan *et al.*, 2011] and 3D seismics [Fault A' of Riedel *et al.*, 2010]. This observation suggests that our assumption of no free gas below the base of GHSZ is acceptable for most of the CDPs. However, a small group of CDPs from 436 to 458 within the fault zone F1 shows an azimuth of $\sim 20^\circ$. It is unlikely that the azimuth of the fault F1 changes drastically within the fault zone; therefore, we propose that the AVA gradient for these CDPs is governed by both the hydrate concentrations and gas saturations. We inverted the AVA parameters for the hydrate concentration and free gas saturation assuming that the azimuth of the fault system is 45° . The estimated hydrate concentration and the gas saturation for these CDPs are close to 20 % and 10 %, respectively.

respectively. Interestingly, the velocity model obtained using unified imaging and waveform inversion [Jaiswal *et al.*, 2012a,b] confirms the presence of free gas in the vicinity of CDP 450.

Gas hydrate may occur within the pore spaces of the sediment matrix (pore-filling) or as fracture-filled deposits. In the present study, we modeled these end member deposits using TPBE and Backus models to estimate the elastic moduli and density for AVA analysis. The anisotropic AVA analysis of the BSR suggests the presence of fracture-filled gas hydrate deposits in the vicinity of the base of the GHSZ. The high resolution X-ray CT (computer tomography) scans and P- and S-wave velocities of the pressure cores (Sites NGHP-01-10/12/13 and 21) [Collett *et al.*, 2008] also suggest that the gas hydrate occurs predominantly in the form of grain-displacing veins (fracture-filled) and negligible concentration may exist in disseminated form (pore-filling). Such negligible pore-filling hydrate may not significantly alter the saturation estimates.

The CDPs from 650 to 800 show class II/III AVA patterns with small-to-moderate normal-incidence reflection coefficients and large negative gradients. Such AVA behavior is predicted neither from the TPBE nor from the Backus model. Interestingly, these CDPs lie in the intersection of two fault systems [Faults A' and B' of Riedel *et al.*, 2010] which may yield a lower anisotropic symmetry such as orthorhombic medium. The AVA pattern for these CDPs may be associated with lower anisotropic media.

7. Conclusions

The AVA of BSRs is an important tool for understanding the distribution of gas hydrate and free gas in the vicinity of GHSZ. The tool is well established for isotropic media where the hydrate is distributed either in pore space or as a load-bearing matrix. In the present study, we analyze multi-channel reflection seismic data in the vicinity of Site NGHP-01-10 to understand the variation in the BSR reflection coefficients for fracture-filled gas hydrate deposit. The AVA of the BSR shows low-to-moderate reflection coefficients (-0.04 to -0.11) at normal-incidence and its absolute magnitude decreases with angle suggesting a class IV AVA pattern. The established isotropic TPBE model fails to reproduce such class IV AVA pattern in the KG offshore basin indicating that the gas hydrate bearing sediment is anisotropic.

We analyze the available anisotropic rock physics models in the KG offshore basin and infer that the anisotropic gas hydrate bearing sediment can be approximated to an HTI medium whose parameters are computed using the Backus averaging technique. Such a model produces azimuthally dependent

reflection coefficients with class IV AVA pattern in the isotropy plane (fracture plane). The positive AVA gradient in the isotropy plane is governed by the velocity of the fast S-wave which is much higher than that predicted from the TPBE model. Using anisotropic AVA, the observed class IV pattern can be modeled for selected CDPs from the inline and crossline seismic profiles.

The AVA of the BSR is analyzed for the inline seismic profile, and hydrate concentration is estimated to be in the range of 5-30 %. The mean azimuth of the major fault systems (F1, F3, and F5) is about 45°, which is close to that interpreted from the 2D and 3D seismic data. The presence of free gas below the GHSZ is negligible for most of the CDPs. However, some CDPs in the vicinity of fault F1 indicate the presence of free gas. The AVA of BSR close to the intersection of the two fault systems (A' and B') shows low-to-moderate normal-incidence reflection coefficient with large negative gradient which cannot be modeled assuming an HTI medium; hence, the medium may be represented by a lower anisotropic symmetry.

Appendix A: Three-Phase Biot-Type equation [Lee and Waite, 2008]

The TPBE model is defined for unconsolidated marine sediments based on the empirical relation between the frame and matrix moduli [Pride, 2003; Pride et al., 2004]. The TPBE is well established for the gas hydrate bearing sediments [Lee and Waite, 2008; Lee and Collett, 2009]. The bulk (k) and shear (μ) moduli of the gas hydrate bearing sediments (GHBS) can be derived from the following relationship:

$$k = k_{ma}(1 - \beta_1) + \beta_1^2 K_{av}, \quad (A1)$$

$$\mu = \mu_{ma}(1 - \beta_2),$$

where

$$\frac{1}{K_{av}} = \frac{(\beta_1 - \phi)}{k_{ma}} + \frac{\phi_w}{k_w} + \frac{\phi_h}{k_h},$$

$$\beta_1 = \frac{\phi_{as}(1 + \alpha)}{(1 + \alpha\phi_{as})}, \beta_2 = \frac{\phi_{as}(1 + \gamma\alpha)}{(1 + \gamma\alpha\phi_{as})}, \text{ and}$$

$$\gamma = \frac{1 + 2\alpha}{1 + \alpha}.$$

The variable α represents the consolidation parameter [Pride *et al.*, 2004] and the subscripts ma , w , and h refer to sediment grain, water and gas hydrate, respectively. The apparent porosity ϕ_{as} can be represented in terms of porosity (ϕ) as,

$$\phi_{as} = \phi_w + \omega\phi_h, \quad (\text{A2})$$

$$\phi_w = (1 - S_h)\phi,$$

$$\phi_h = S_h\phi,$$

where S_h is the gas hydrate saturation. The parameter ω accounts for the reduced impact of hydrate formation relative to compaction in terms of stiffening the host sediments framework [Lee and Waite, 2008; Lee and Collett, 2009]. Generally, a value of $\omega=0.12$ is used for modeling the velocities of GHBS. The bulk density (ρ_b) of GHBS is given by,

$$\rho_b = (1 - \phi)\rho_{ma} + (1 - S_h)\phi\rho_w + \rho_h\phi S_h \quad (\text{A3})$$

The consolidation parameter α depends on the effective pressure (p) and degree of consolidation [Lee and Waite, 2008],

$$\alpha_i = \alpha_o (p_o / p_i)^{1/3} \approx \alpha_o (d_o / d_i)^{1/3}, \quad (\text{A4})$$

where α_o is the consolidation parameter at the effective pressure p_o or depth d_o and α_i is the consolidation parameter at the effective pressure p_i or depth d_i . The sediment matrix is assumed to be 60 % clay and 40 % sand in the KG offshore basin [Collett *et al.*, 2008]. The bulk modulus, shear modulus and density for sand (quartz), clay, gas hydrate and pore water are same as that used by Lee and Collett [2009].

Appendix B: Effect of shear wave velocity on the BSR gradient

The variation in the shear wave velocity has a large effect on the AVA gradient [Castagna *et al.*, 1998]. The effect of shear wave velocity on the AVA gradient can be studied using approximate P-wave reflection coefficients in isotropic media (R_p) [e.g., Rüger, 1998].

$$R_p^{iso}(i) = 1/2 \frac{\Delta Z}{Z} + 1/2 \left\{ \frac{\Delta \alpha}{\alpha} - \left(\frac{2\bar{\beta}}{\alpha} \right)^2 \frac{\Delta G}{G} \right\} \sin^2 i + 1/2 \frac{\Delta \alpha}{\alpha} \sin^2 i \tan^2 i, \quad (\text{B1})$$

where i is the angle of incidence. The P- and S-wave velocities are defined by α and β , respectively. The average P- and S-wave velocities of the upper and lower layers are given by $\bar{\alpha}$ and $\bar{\beta}$, respectively while the differences are denoted by $\Delta\alpha$ and $\Delta\beta$. The P-wave impedance is represented as $Z = \rho\alpha$. Similarly, \bar{Z} and ΔZ are the average and difference of the impedance. The shear modulus is given by $G = \rho\beta^2$ and its average and difference are given by \bar{G} and ΔG . The parameter ρ represents the density.

Let us consider a two layer model where the upper layer represents GHBS and the lower layer represents water saturated background sediment. The gradient (B) in an isotropic media can be approximated as,

$$B = \left\{ \frac{\Delta\alpha}{\alpha} - \left(\frac{2\bar{\beta}}{\alpha} \right)^2 \frac{\Delta G}{G} \right\}. \quad (\text{B2})$$

The approximate condition for zero-gradient ($B=0$) is derived assuming constant density, as the density of GHBS is close to that of the background sediment,

$$\begin{aligned} \left| \left(\frac{2\bar{\beta}}{\alpha} \right)^2 \frac{\Delta G}{G} \right| &= \left| \frac{\Delta\alpha}{\alpha} \right| \\ \Rightarrow \left| \frac{8\bar{\beta}}{\alpha} \right| &= \left| \frac{\Delta\alpha}{\Delta\beta} \right| \end{aligned} \quad (\text{B3})$$

The following approximate condition needs to be satisfied for class IV AVA gradient ($B > 0$),

$$\left| \frac{8\bar{\beta}}{\alpha} \right| > \left| \frac{\Delta\alpha}{\Delta\beta} \right| \quad (\text{B4})$$

Appendix C: Backus averaging technique for seismic anisotropy

The Backus model represents the stratified heterogeneous media as a homogeneous anisotropic medium. It is valid when the thicknesses of the stratified layers are less than the seismic wavelength [Backus, 1962]. The coefficients of the stiffness matrix of the effective transversely isotropic (TI) medium with symmetry axis oriented perpendicular to the layers are given by,

$$\begin{aligned}
C_{11} &= \left\langle 4\rho V_s^2 \left(1 - \frac{V_s^2}{V_p^2}\right) \right\rangle + \left\langle 1 - 2\frac{V_s^2}{V_p^2} \right\rangle^2 \left\langle (\rho V_p^2)^{-1} \right\rangle^{-1}, \\
C_{12} &= \left\langle 2\rho V_s^2 \left(1 - \frac{2V_s^2}{V_p^2}\right) \right\rangle + \left\langle 1 - 2\frac{V_s^2}{V_p^2} \right\rangle^2 \left\langle (\rho V_p^2)^{-1} \right\rangle^{-1}, \\
C_{33} &= \left\langle (\rho V_p^2)^{-1} \right\rangle^{-1}, \\
C_{13} &= \left\langle 1 - 2\frac{V_s^2}{V_p^2} \right\rangle^2 \left\langle (\rho V_p^2)^{-1} \right\rangle^{-1}, \\
C_{44} &= \left\langle (\rho V_s^2)^{-1} \right\rangle^{-1}, \\
C_{66} &= \left\langle \rho V_s^2 \right\rangle,
\end{aligned} \tag{C1}$$

where ρ is the density and V_P , V_S are P- and S-wave velocities of the representative isotropic medium. The symbol $\langle \cdot \rangle$ represents the volumetric average of the individual layers. The direction of the symmetry axis is assumed to be vertical to represent the stiffness matrix.

Acknowledgements

We thank the Director, CSIR-National Institute of Oceanography (NIO) for supporting this study. We also extend our sincere thanks to the Director General, Directorate General of Hydrocarbons (DGH) and Oil and Natural Gas Corporation Limited (ONGC) for providing valuable seismic data, and A. V. Sathe (ONGC) and M. V. Lall (DGH) for their suggestions. We also thank the Department of Science & Technology, New Delhi, India for financial support through an award of INSPIRE fellowship. We would like to thank Dr. Priyank Jaiswal and an anonymous reviewer for their constructive comments/suggestions which have improved the quality of the manuscript. We also thank the associate editor for efficient handling of the manuscript. This is CSIR-NIO contribution no. ---.

References

- Andreassen, K., P. E. Hart, and A. Grantz (1995), Seismic studies of a bottom simulating reflection related to gas hydrate beneath the continental margin of the Beaufort Sea, *J. Geophys. Res.*, *100*(B7), 12659–12673.
- Andreassen, K., P. E. Hart, and M. MacKay (1997), Amplitude versus offset modeling of the bottom simulating reflection associated with submarine gas hydrates, *Mar. Geol.*, *137*, 25–40.
- Backus, G. E. (1962), Long-wave elastic anisotropy produced by horizontal layering, *J. Geophys. Res.*, *67*(11), 4427–4440, doi: 10.1029/JZ067i011p04427.

- Bakulin, A., V. Grechka, and I. Tsvankin (2000a), Estimation of fracture parameters from reflection seismic data—Part I: HTI model due to a single fracture set. *Geophysics*, 65(6), 1788–1802.
- Bakulin, A., V. Grechka, and I. Tsvankin (2000b), Estimation of fracture parameters from reflection seismic data—Part III: Fractured models with monoclinic symmetry. *Geophysics*, 65(6), 1818–1830.
- Bastia, R. (2007), *Geologic Settings and Petroleum Systems of India's East Coast Offshore Basins: Concepts and Applications*, Technology Publication, Dehradun, India.
- Carcione, J. M., and U. Tinivella (2000), Bottom-simulating reflectors: seismic velocities and AVO effects, *Geophysics*, 65(1), 54–67.
- Castagna, J. F., H. W. Swan, and D. J. Foster (1998), Framework for AVO gradient and intercept interpretation, *Geophysics*, 63(3), 948–956.
- Collett, T., M. Riedel, J. Cochran, R. Boswell, J. Presley, P. Kumar, A. Sathe, A. Sethi, M. V. Lall, V. Sibal, and the NGHP Expedition 01 Scientists (2008), *Indian National Gas Hydrate Program Expedition 01 Initial Reports*, Directorate General of Hydrocarbons, Noida.
- Cook, A. E., B. I. Anderson, A. Malinverno, S. Mrozewski, and D. S. Goldberg (2010), Electrical anisotropy due to gas hydrate-filled fractures, *Geophysics* 75(6), F173–F185.
- Dallimore, S. R., T. Uchida, and T. S. Collett (1999), *Scientific results from JAPEX/JNOC/GSC Mallik 2L-38 gas hydrate research well, Mackenzie Delta, northwest territories, Canada*, Bulletin of Geological Survey of Canada, 544, 403pp.
- Dewangan, P., and T. Ramprasad (2007), Velocity and AVO analysis for the investigation of gas hydrate along a profile in the western continental margin of India, *Mar. Geophys. Res.*, 28(3), 201–211.
- Dewangan, P., T. Ramprasad, M. V. Ramana, A. Mazumdar, M. Desa, and F. Badesab (2010), Seabed morphology and gas venting features in the continental slope region of Krishna-Godavari basin, Bay of Bengal: implications in gas-hydrate exploration. *Mar. Petrol. Geol.*, 27(7), 1628–1641.
- Dewangan, P., G. Sriram, T. Ramprasad, M. V. Ramana, and P. Jaiswal (2011), Fault system and thermal regime in the vicinity of site NGHP-01-10, Krishna-Godavari basin, Bay of Bengal, *Mar. Petrol. Geol.*, 28(10), 1899–1914.
- Dvorkin, J., M. Prasad, and A. Sakai (1999), Elasticity of Marine Sediments: Rock Physics Modeling, *Geophys. Res. Lett.*, 26(12), 1781–1784.
- Ecker, C., J. Dvorkin, and A. Nur (1998), Sediments with gas hydrates: Internal structure from seismic AVO, *Geophysics*, 63(5), 1659–1669.
- Gajewski, D., and I. Pšenčík (1987), Computation of high frequency seismic wavefields in 3-D laterally inhomogeneous anisotropic media, *Geophys. J. Roy. Astr. Soc.*, 91(2), 383–412.
- Ghosh, R., K. Sain, and M. Ojha (2010), Effective medium modeling of gas hydrate-filled fractures using the sonic log in the Krishna-Godavari basin, offshore eastern India, *J. Geophys. Res.*, 115, B06101, doi: 10.1029/2009JB006711.

- Gupta, S. K. (2006), Basin architecture and petroleum system of Krishna Godavari Basin, east coast of India, *The Leading Edge*, 25, 830.
- Hardage, B. A., P. E. Murray, and D. C. Sava (2007), Combining Multicomponent seismic attributes, new rock physics models, and In situ data to estimate gas-hydrate concentrations in Deep-Water, Near-Seafloor Strata of the Gulf of Mexico, *Technical Report*, Bureau of Economic Geology, The University of Texas at Austin University Station.
- Helgerud, M. B., J. Dvorkin, A. Nur, A. Sakai, and T. Collett (1999), Elastic-wave velocity in marine sediments with gas hydrates: Effective medium modeling, *Geophys. Res. Lett.*, 26(13), 2021–2024, doi: 10.1029/1999GL900421.
- Hyndman, R. D., and G. D. Spence (1992), A seismic study of methane hydrates marine bottom simulating reflectors, *J. Geophys. Res.*, 97(B5), 6683–6698, doi:10.1029/92JB00234.
- Jaiswal, P., P. Dewangan, T. Ramprasad, and C. A. Zelt (2012a), Seismic characterization of hydrates in faulted, fine-grained sediments of Krishna-Godavari basin: Unified imaging, *J. Geophys. Res.*, 117, B04306, doi:10.1029/2011JB009024.
- Jaiswal, P., P. Dewangan, T. Ramprasad, and C. A. Zelt (2012b), Seismic characterization of hydrates in faulted, fine-grained sediments of Krishna-Godavari basin: Full waveform inversion, *J. Geophys. Res.*, 117, B10305, doi:10.1029/2012JB009201.
- Jakobsen, M., J. A. Hudson, T. A. Minshull, and S. C. Singh (2000), Elastic properties of hydrate-bearing sediment using effective medium theory, *J. Geophys. Res.*, 105(B1), 561–577, doi:10.1029/1999JB900190.
- Jilek, P. (2001), Modeling and Inversion of Converted-Wave reflection coefficients in Anisotropic Media: A tool for Quantitative AVO Analysis, PhD thesis, CWP, Colorado School of Mines, Golden, Colorado, USA.
- Johansen, T. A., B. O. Ruud, and M. Jakobsen (2004), Effect of grain scale alignment on seismic anisotropy and reflectivity of shales, *Geophys. Prospect.*, 52(2), 133–149.
- Kumar, D., M. K. Sen, N. L. Bangs, C. Wang, and I. Pecher (2006), Seismic anisotropy at Hydrate Ridge, *Geophys. Res. Lett.*, 33, L01306, doi: 10.1029/2005GL023945.
- Lee, M. W., D. R. Hutchinson, T. S. Collett, and W. P. Dillon (1996), Seismic velocities for hydrate-bearing sediments using weighted equation, *J. Geophys. Res.*, 101(B9), 20347–20358, doi:10.1029/96JB01886.
- Lee, M. W., and T. S. Collett (2001), Elastic properties of gas hydrate-bearing sediments, *Geophysics*, 66(3), 763–771.
- Lee, M. W. (2004), Elastic velocities of partially gas-saturated unconsolidated sediments, *Mar. Petrol. Geol.*, 21(6), 641–650.
- Lee, M. W. (2008), Models for gas hydrate-bearing sediments inferred from hydraulic permeability and elastic velocities, *U.S. Geol. Surv. Sci. Invest. Rep.*, 2008-5219, 15 pp.
- Lee, M. W., and W. F. Waite (2008), Estimating pore-space gas hydrate saturations from well-log acoustic data, *Geochem. Geophys. Geosyst.*, 9, Q07008, doi:10.1029/2008GC002081.

- Lee, M. W., and T. S. Collett (2009), Gas hydrate saturations estimated from fractured reservoir at Site NGHP-01-10, Krishna-Godavari Basin, India, *J. Geophys. Res.*, *114*, B07102, doi:10.1029/2008JB006237.
- Matsumoto, R., Y. Takedomi, and H. Wassada (2001), Exploration of Marine Gas Hydrates in Nankai Trough, Offshore Central Japan, *AAPG Annual Convention, Official Program 10*, p. A128.
- Müller, C., C. Bönemann, and S. Neben (2007), AVO study of a gas-hydrate deposit, offshore Costa Rica, *Geophys. prospect.*, *55*(5), 719–735.
- Newman, P. (1973), Divergence effects in a layered earth, *Geophysics*, *38*(3), 481–488.
- Ojha, M., and K. Sain (2007), Seismic velocities and quantification of gas hydrates from AVA modeling in the western continental margin of India, *Mar. Geophys. Res.*, *28*, 101–107.
- Ostrander, W. J. (1984), Plane-wave reflection coefficients for gas sands at non-normal angles of incidence, *Geophysics*, *49*, 1637–1649.
- Pride, S. R. (2003), Relationships between seismic and hydrological properties, in *Hydrogeophysics*, Kluwer Acad., New York, pp. 1–31.
- Pride, S. R., J. G. Berryman, and J. M. Harris (2004), Seismic attenuation due to wave-induced flow, *J. Geophys. Res.*, *109*, B01201, doi: 10.1029/2003JB002639.
- Ramana, M. V., T. Ramprasad, and M. Desa (2001), Seafloor spreading magnetic anomalies in the Enderby Basin, East Antarctica, *Earth Planet. Sci. Lett.*, *191*, 241–255.
- Ramana M. V., T. Ramprasad, M. Desa, A. V. Sathe, and A. K. Sethi (2006), Gas hydrate-related proxies inferred from multidisciplinary investigations in the Indian offshore areas, *Curr. Sci.*, *91*(2), 183–189.
- Ramana, M. V., T. Ramprasad, A. L. Paropkari, D. V. Borole, B. Ramalingeswara Rao, S. M. Karisiddaiah, M. Desa, M. Kocherla, H. M. Joao, P. Lokabharati, M. J. Gonsalves, J. N. Pattan, N. H. Khadge, C. Prakash Babu, A. V. Sathe, P. Kumar, and A. K. Sethi (2008), Multidisciplinary investigations exploring indicators of gas hydrate occurrence in the Krishna-Godavari basin offshore, east coast of India, *Geo-Mar. Lett.*, *29*(1), 25–38.
- Rao, G. N. (2001), Sedimentation, stratigraphy, and petroleum potential of Krishna-Godavari basin, east coast of India, *AAPG Bulletin*, *85*, 1623–1643.
- Rao, G. N., and K. S. Mani (1993), A study on generation of abnormal pressures in Krishna-Godavari basin, *Indian Journal of Petroleum Geology*, *2*, 20–30.
- Riedel, M., T. S. Collett, P. Kumar, A. V. Sathe, and A. Cook (2010), Seismic imaging of a fractured gas hydrates system in the Krishna-Godavari Basin offshore India, *Mar. Petrol. Geol.*, *27*(7), 1476–1493.
- Rüger, A. (1997), P-wave reflection coefficients for transversely isotropic models with vertical and horizontal axis of symmetry, *Geophysics*, *62*(3), 713–722.
- Rüger, A. (1998), Variation of P-wave reflectivity with offset and azimuth in anisotropic media, *Geophysics*, *63*, 935–947.

- Sava, D. C., and B. A. Hardage (2006), Rock physics characterization of hydrate-bearing deepwater sediments, *The Leading Edge*, 25(5), 616–619.
- Scotese, C. R., L. M. Gahagan, and R. L. Larson (1988), Plate tectonic reconstructions of the Cretaceous and Cenozoic ocean basins, *Tectonophysics*, 155, 27–48.
- Singh, S. C., T. A. Minshull, and G. D. Spence (1993), Velocity structure of a gas hydrate reflector, *Science*, 260(5105), 204–207.
- Shankar, U., and M. Riedel (2010), Seismic and heat flow constraints from the gas hydrate system in the Krishna-Godavari Basin, India, *Mar. Geol.*, 276(1), 1–13, doi:10.1016/j.margeo.2010.06.006.
- Sheriff, R. E., and L. P. Geldart (1982), *Exploration seismology: History, theory, and data acquisition*, Cambridge Univ. Press, v. 1.
- Shuey, R. T. (1985), A simplification of the Zoeppritz equations, *Geophysics*, 50(4), 609–614.
- Sloan, E. D (1990), *Clathrate Hydrates of Natural Gases*, Marcel Dekker, Inc., New York. 641pp.
- Thomsen, L. (1986), Weak elastic anisotropy, *Geophysics*, 51(10), 1954–1966.
- Thomsen, L. (1988), Reflection seismology over azimuthally anisotropic media, *Geophysics*, 53(3), 304–313.
- Tsvankin, I. (1997), Reflection moveout and parameter estimation for horizontal transverse isotropy, *Geophysics*, 62(2), 614–629.
- Tsvankin, I. (2001), *Seismic signatures and analysis of reflection data in anisotropic media*, Elsevier Science Ltd, Oxford, 436pp.
- Ursin, B., and K. Hokstad (2003), Geometrical spreading in a layered transversely isotropic medium with vertical symmetry axis, *Geophysics*, 68(6), 2082–2091.
- Vavryčuk, V. and I. Pšenčík (1998), PP-wave reflection coefficients in weakly anisotropic elastic media, *Geophysics*, 63(6), 2129–2141.
- Vavryčuk, V. (1999), Weak-contrast reflection/transmission coefficients in weakly anisotropic elastic medium: P-wave incidence, *Geophys. J. Int.*, 138, 553–562, doi: 10.1046/j.1365-246X.1999.00890.x.
- Warner, M. (1990), Absolute reflection coefficients from deep seismic reflections, *Tectonophysics*, 173(1), 15–23.
- White, J. E. (1965), *Seismic Waves—Radiation, Transmission, and Attenuation*, McGraw-Hill, New York, 320pp.
- Xu, X., I. Tsvankin, and A. Pech (2005), Geometrical spreading of P-waves in horizontally layered, azimuthally anisotropic media, *Geophysics*, 70(5), D43–D53.
- Zoeppritz, K. (1919), On the reflection and penetration of seismic waves through unstable layers, in *Goettinger Nachr (ed) Erdbebenwellen VIII B, 1*, 66–84.

Figures caption

Figure 1. Location map of the study area in the KG offshore basin along with the regional tectonics setting showing the horst and graben structures [Rao, 2001; Bastia, 2007] the onshore KG basin, Bay of Bengal. The zoom out of the study area with multibeam bathymetry is shown in Figure 1b. The seismic lines are illustrated on the bathymetry map. The seismic lines are annotated with CDP numbers and the Sites NGHP-01-10 and NGHP-01-03 are highlighted on the map. The interpreted fault system (F1-F4) and its symmetric-axis and isotropy planes are marked on the map [Dewangan *et al.*, 2011]. The faults A' and B' are interpreted from 3D seismic data [Riedel *et al.*, 2010]. The azimuths of the seismic profiles with respect to the symmetry-axis of the fault system are shown in Figure 1b. The CDPs showing the class IV AVA pattern are marked in dark gray.

Figure 2. Seismic profiles along the NNW-SSE direction (inline) and ENE-WSW direction (crossline): a) Time-migrated stacked multi-channel seismic data of inline seismic profile, b) Time-migrated stacked multi-channel seismic data of crossline seismic profile. The seafloor and BSR reflections, the interpreted fault system and the location of Site NGHP-01-10 are marked on the figure.

Figure 3. AVO analysis of BSR from the inline seismic profile. a) The near-offset stack (75-295 m) showing the zones of strong BSR (marked in black ellipse) and weak BSR (marked in stippled black ellipse), b) The far-offset stack (1295-1545 m) highlighting weak BSR (black) and strong BSR (stippled black). The gathers at CDPs 430 and 835 are shown as examples of class IV AVA of BSR in Figure 5.

Figure 4. Similar to Figure 3 showing AVO analysis of BSR from the crossline seismic profile. a) The near-offset stack (75-295 m) with strong BSR and b) The far-offset stack (1295-1545 m) with weak BSR are highlighted. The gathers at CDPs 520 and 715 are shown as examples of class IV AVA of BSR in Figure 5. The CDP gather 715 lies in the vicinity of Site NGHP-01-10.

Figure 5. Seafloor and BSR reflection coefficients as a function of incidence angle in the KG offshore basin after applying isotropic correction for AVA. The seafloor AVA shows a gradual decrease in amplitude with incidence angle and can be modeled using the Zoeppritz equations. The magnitude of BSR amplitude decreases systematically with angle showing class IV AVA pattern. The AVA pattern is fitted with three-term Shuey's approximation to the Zoeppritz equations [Shuey, 1985].

Figure 6. a) The estimated P- and S-wave velocities from TPBE model [Lee and Collett, 2009] as a function of gas hydrate saturation. b) Exact P-wave reflection coefficient is shown as a function of incidence angle for different gas hydrate saturations assuming no free gas below the GHSZ. The TPBE model predicts class III AVA of BSR for different hydrate saturations.

Figure 7. The AVA gradient is shown as a function of P- and S-wave velocity contrasts ($\Delta\alpha$ and $\Delta\beta$). The approximate condition for zero-gradient (equation B3) is shown by solid line with cross. The estimated AVA gradients from the seismic data are shown as stars.

Figure 8. The stacked migrated time section and a CDP gather in the vicinity of Site NGHP-01-03. a) The seismic data show a BSR which is probably formed due to the presence of free gas below the base of the GHSZ. b) The hyperbolic NMO-corrected CDP gather highlighting the reflection of seafloor, BSR and a deeper horizon (dotted White). Non-hyperbolic moveout of BSR predicted from the parameters of VTI medium [Ghosh et al., 2010] is shown as a black line after hyperbolic NMO-correction.

Figure 9. Generic Thomsen's anisotropic parameters of the HTI medium obtained from Backus model are shown as a function of hydrate concentration. a) The vertical and the horizontal P-wave velocities (α and α^\perp) for the HTI medium and P-wave velocity estimated from the TPBE model (α_{iso}), b) The fast (β) and slow (β^\perp) S-wave velocities propagating in vertical direction and polarized in the isotropy and symmetric-axis planes, respectively. The S-wave velocity estimated from the TPBE model (β_{iso}), c) shear wave splitting parameter gamma (γ), d) epsilon ($\epsilon^{(v)}$), d) delta ($\delta^{(v)}$), and e) gamma ($\gamma^{(v)}$) in HTI medium.

Figure 10. Exact P-wave reflection coefficients in HTI medium as a function of incidence group and phase angles for different gas hydrate concentrations. a) P-wave reflection coefficients in HTI medium in the symmetry-axis plane for gas hydrate concentrations (10 - 40 %) without free gas below the GHSZ, b) P-wave reflection coefficients in HTI medium in the isotropy plane for the same gas hydrate concentrations without free gas showing prominent class IV AVA pattern. The incidence phase and group angles are same in the isotropy plane of HTI medium.

Figure 11. Relative anisotropic geometrical spreading correction for BSR computed in the a) symmetry-axis, b) 45° azimuthal and c) isotropy planes for different hydrate concentrations using equation (7).

Figure 12. The class IV AVA of BSR in the KG offshore basin after correcting for the effect of anisotropy wave propagation on the BSR amplitudes. The P-wave BSR reflection coefficients for the inline CDPs 835 and 430 are shown in panels (a) and (c), respectively. Similarly, the reflection coefficients of crossline CDPs 715 and 520 are shown in (b) and (d). The observed class IV AVA of BSR can be modeled as a function of group angle using an azimuth of 45° and a realistic hydrate concentration (10-30 %) assuming no free gas below the base of GHSZ.

Figure 13. The computed class IV AVA of BSR due to the fracture-filled gas hydrate (HTI medium) and underlying fracture-filled free gas bearing sediment (HTI medium) for different hydrate concentrations and free gas saturations; a) without free gas, b) with 5 % saturation, and c) with 10 % saturation.

Figure 14. Anisotropic AVA analysis of the BSR from the inline seismic profile. a) interpreted inline seismic section with marked seafloor, BSR and fault zones; b) intercept (A, inverted triangles) and c) gradient (B, triangles) of BSR estimated by fitting the reflection coefficients by a two-term Shuey's approximation; d) gas hydrate concentration (equivalent to fracture density, inverted triangles) and e) azimuth of the fault system with respect to the seismic profile (triangles) estimated after anisotropic AVA analysis assuming no free gas below the GHSZ. The boxes (marked in red) indicate the gas hydrate concentration estimated assuming a fracture azimuth of 45° . The intercepts and gradients which can be modeled neither by using the TPBE nor by using the Backus model are shown in blue.

Figure.1.

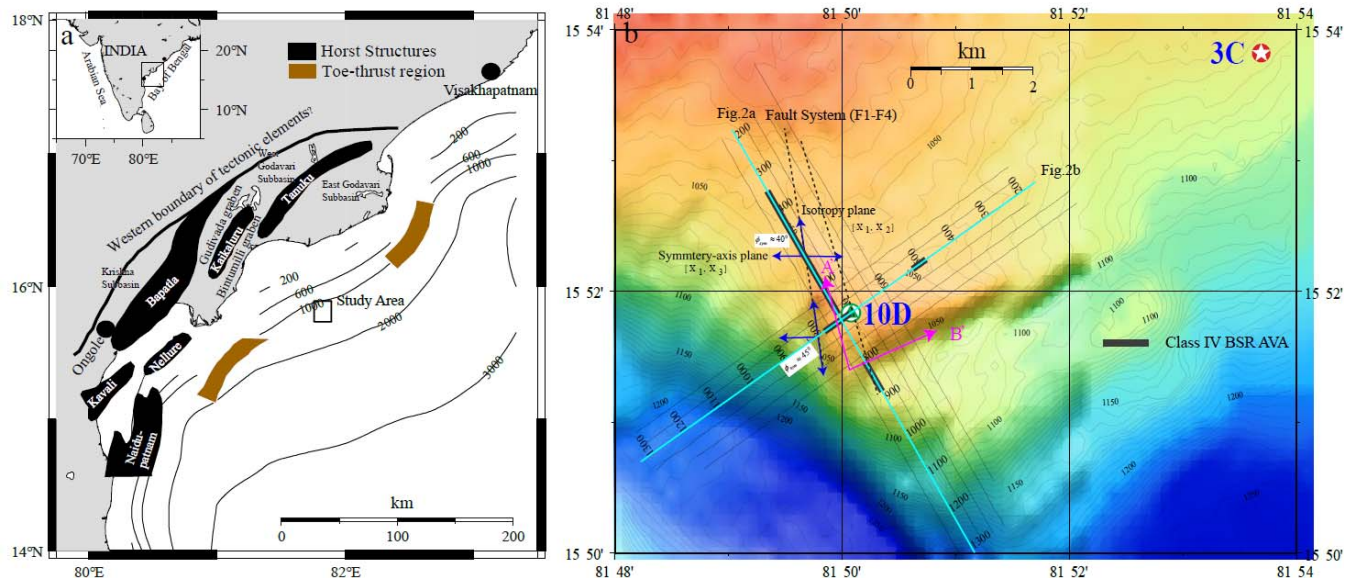


Figure.2

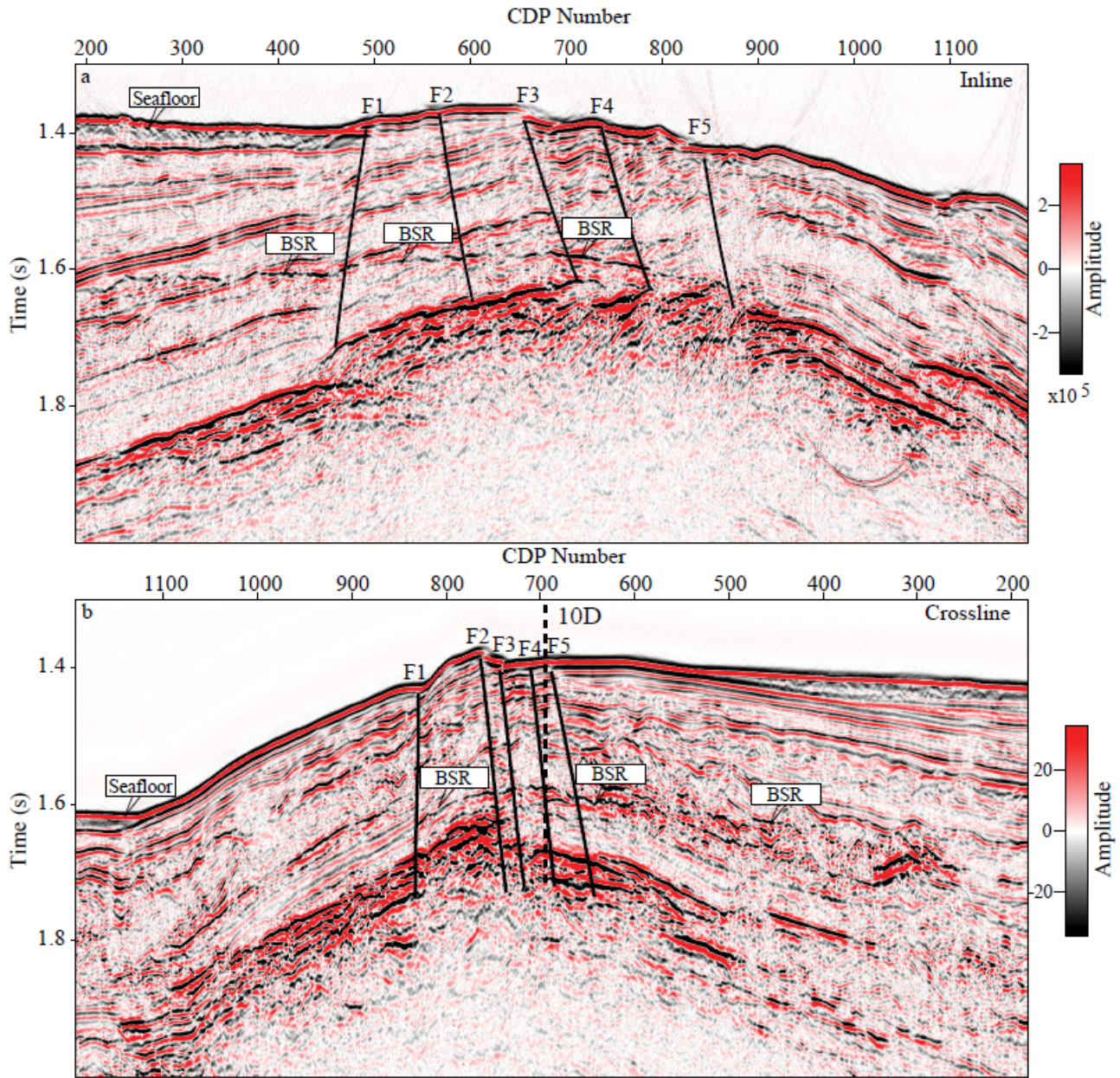


Figure.3

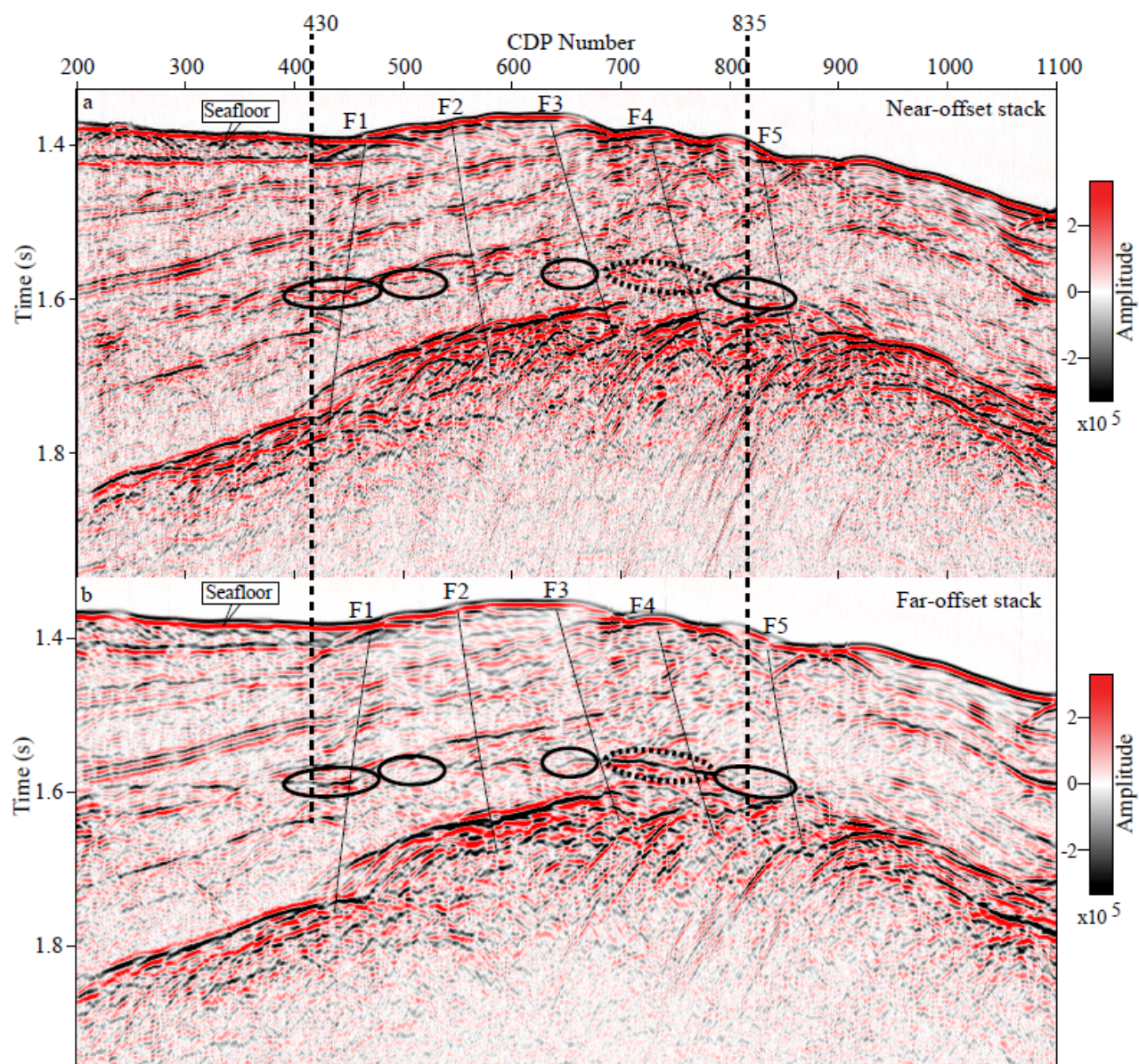


Figure.4

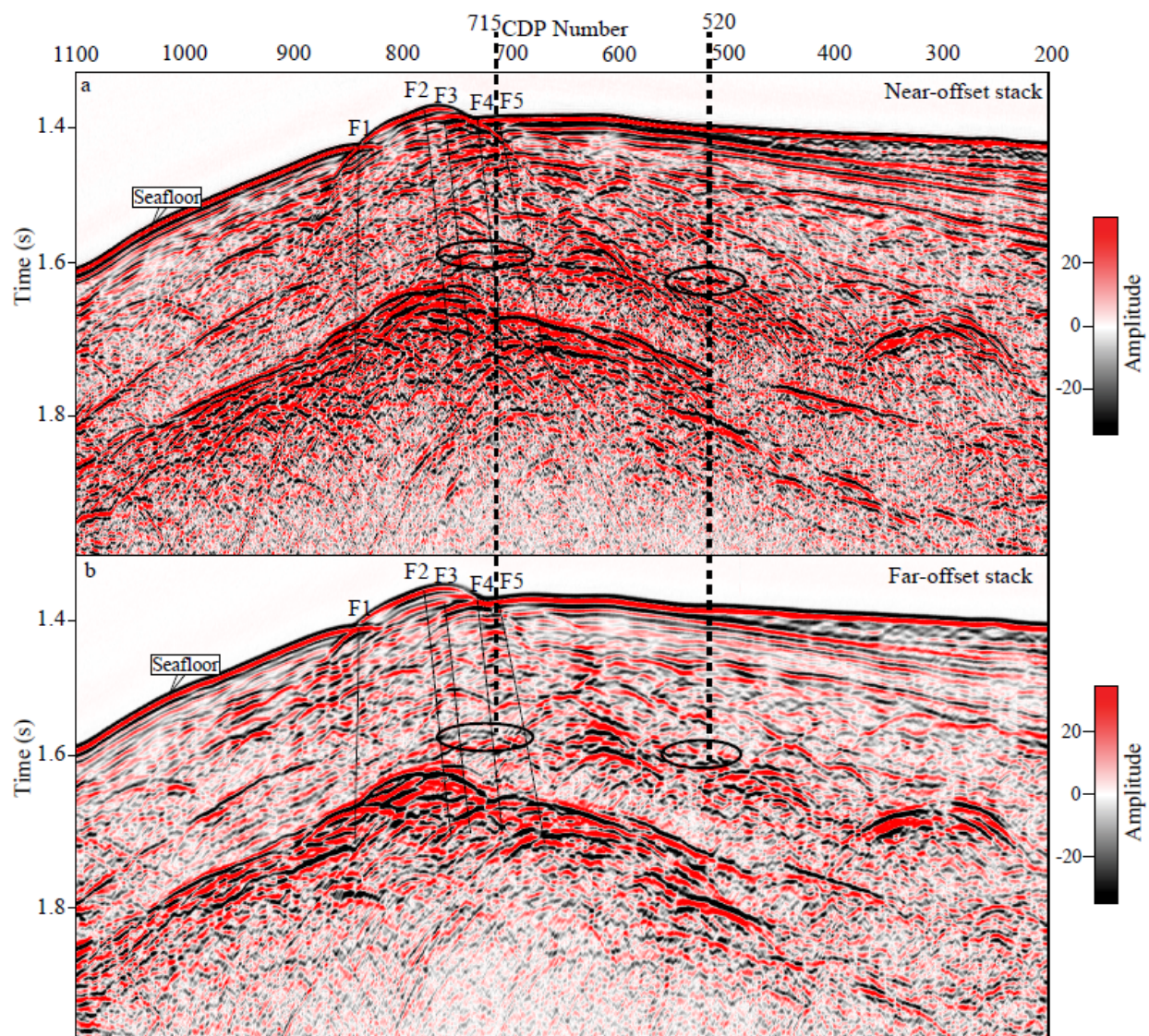


Figure.5.

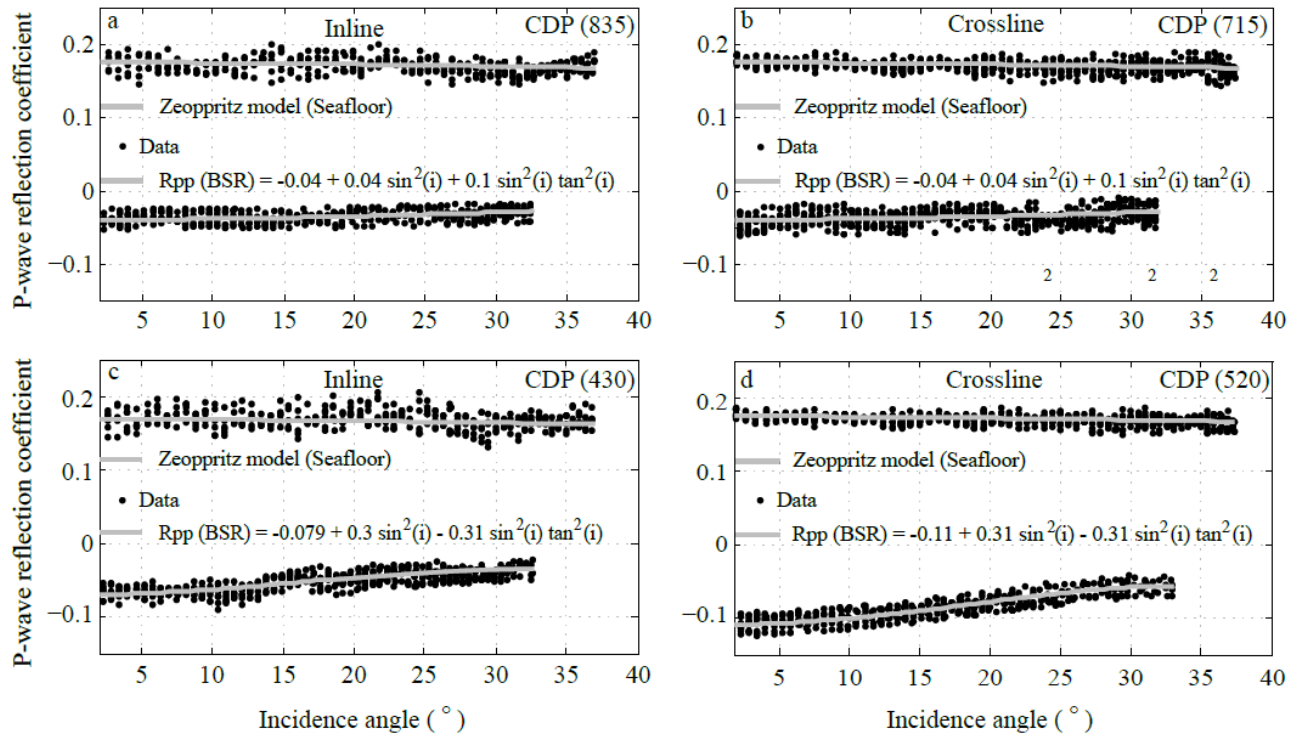


Figure.6

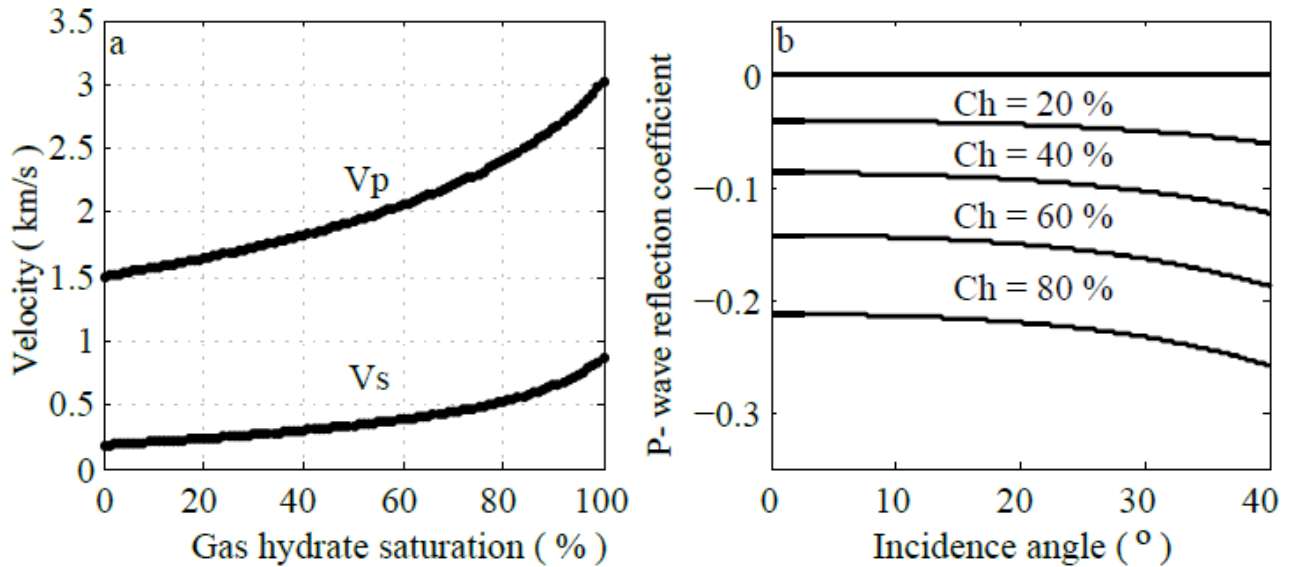


Figure.7

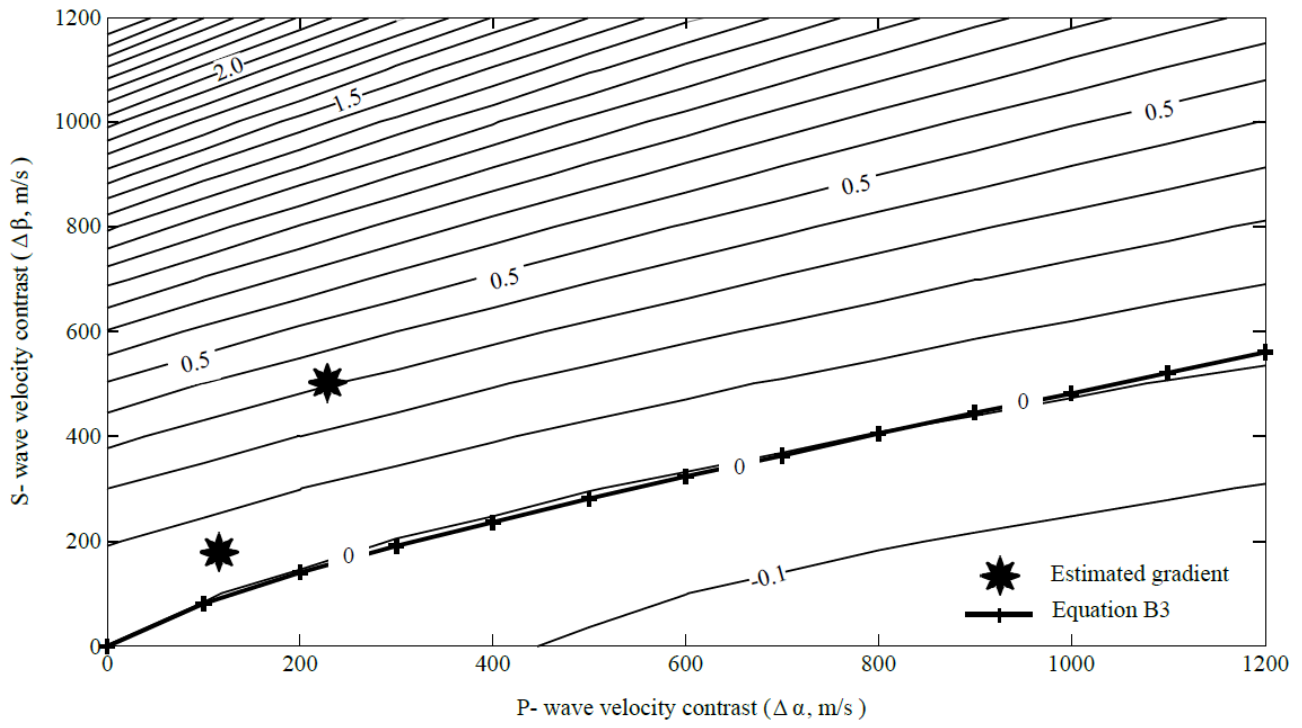


Figure.8

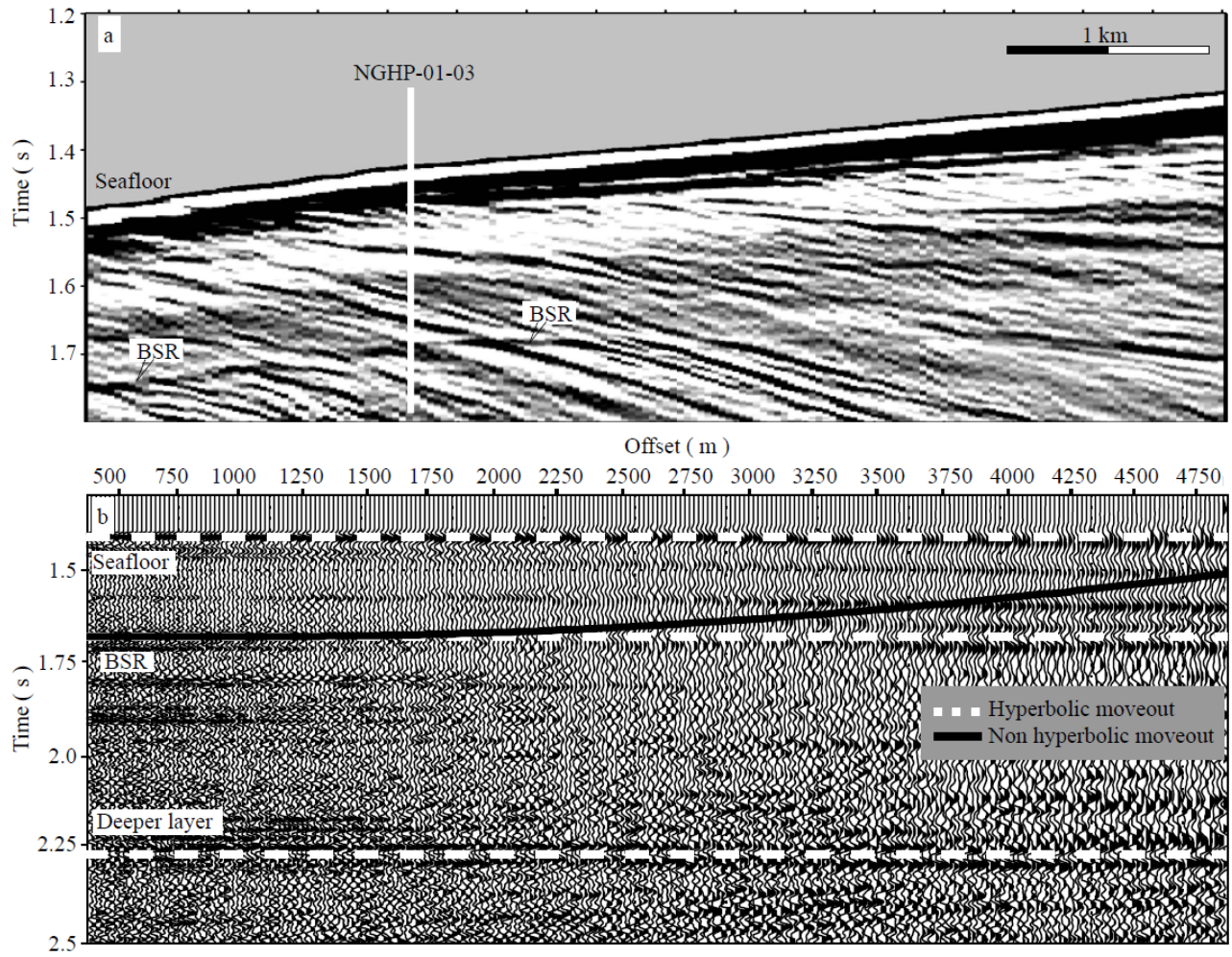


Figure.9

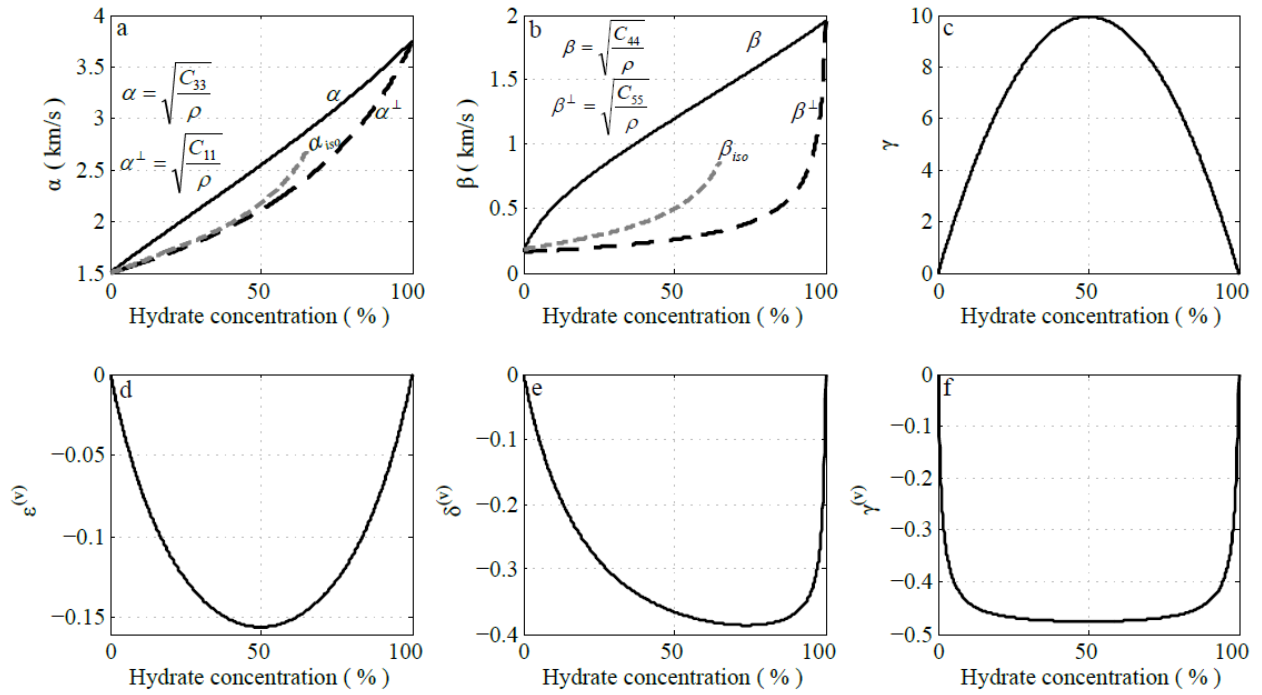


Figure.10

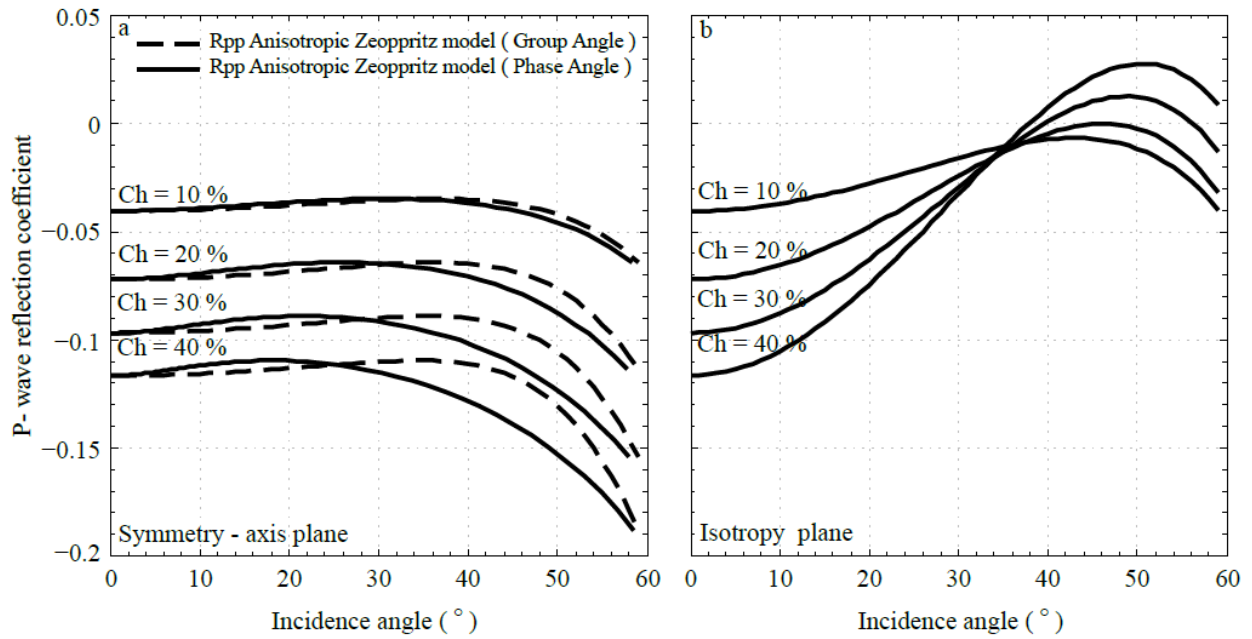


Figure.11

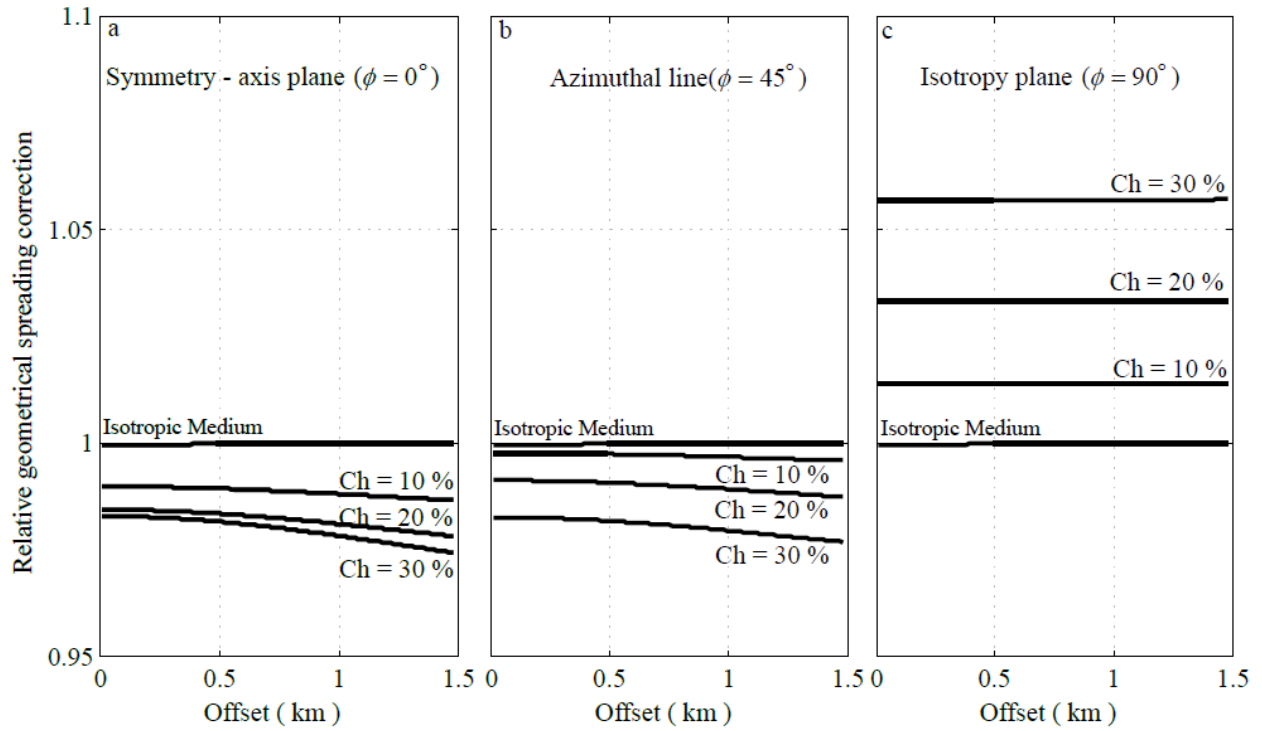
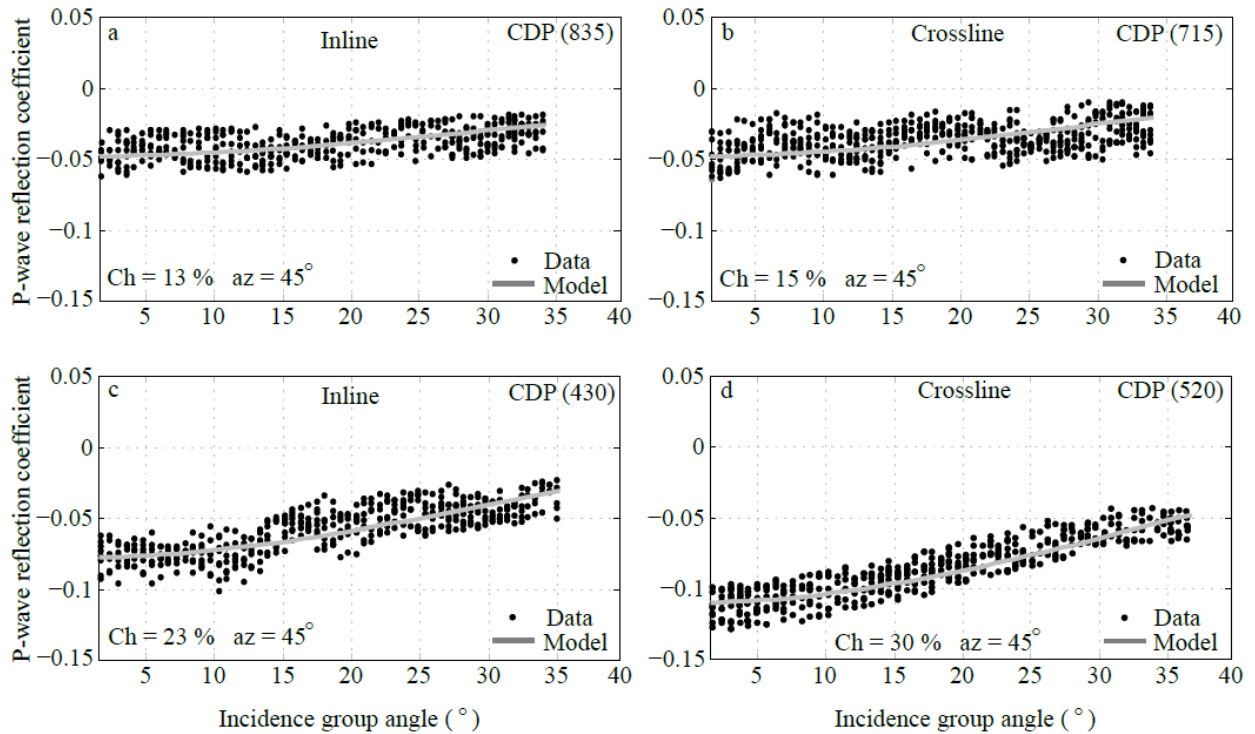


Figure.12



Figur.13

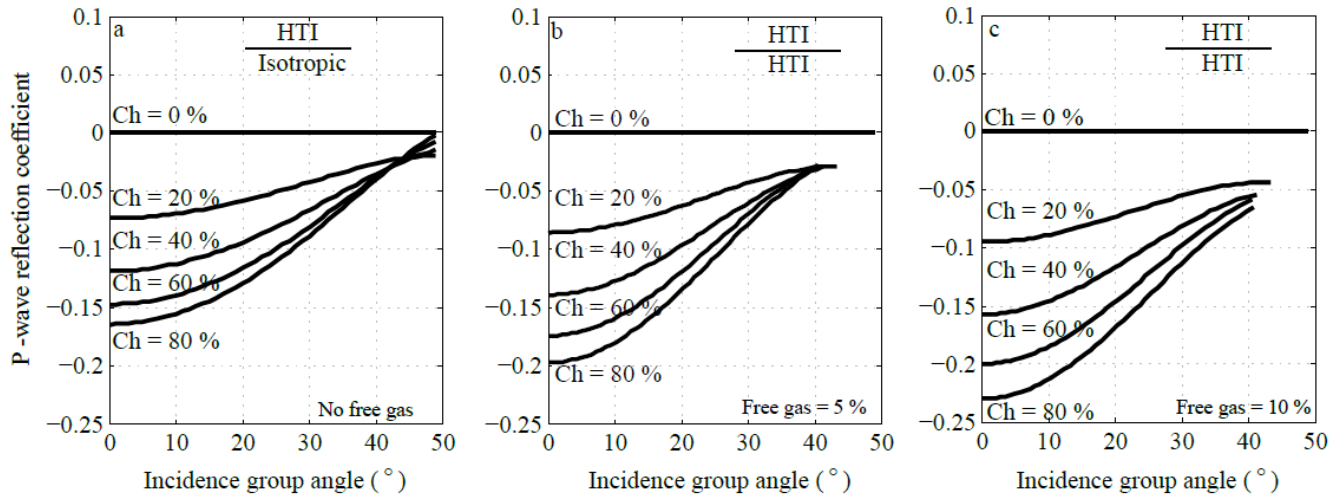


Figure.14

